Field Monitoring and Numerical Investigation of Constrained Layer Damper for Mitigation of Wind-induced Vibration of High Mast Illumination Poles

By

Mona Shaheen
B.Sc., Jordan University of Science and Technology, 2017

Submitted to the graduate degree program in Civil, Environmental, and Architectural Engineering and the Graduate Faculty of the University of Kansas in partial fulfillment of the requirements for the degree of Master of Science in Civil Engineering.

Chair: Jian Li, Ph.D., P.E.

Caroline Bennett, Ph.D., P.E.

William Collins, Ph.D., P.E.

Date Defended: November 18, 2022

The thesis committee for Mona Shaheen certifies that this is the approved version of the following thesis:

Field Monitoring and Numerical Investigation of Constrained Layer Damper for Mitigation of Wind-induced Vibration of High Mast Illumination Poles

Chair: Jian Li, Ph.D., P.E.

Date Approved: December 13, 2022

Abstract

High-mast illumination poles (HMIP) are tall and slender structures with low inherent damping. The Kansas Department of Transportation (KDOT) discovered premature cracking near the handhole of several HMIPs in Western Kansas. In addition, multiple video recordings captured significant HMIP vibrations under high wind. This thesis investigates the mechanism of wind-induced vibrations of HMIPs and the potential of using a constrained layer damper (CLD) to mitigate such vibrations.

To examine the underlying mechanism of the wind-induced vibrations of the HMIP structures, the fundamental natural frequencies were extracted from the recorded videos using computer vision algorithms and signal processing. Finite element modeling was then used to confirm that the recorded vibration is dominated by the first bending mode. Subsequently, a 100-ft-tall HMIP in west Kansas was selected for long-term vibration monitoring using wireless smart sensors. Data analysis with the long-term monitoring data indicates that buffeting-induced vibration was the leading cause of the excessive vibrations of the monitored HMIP. This finding leads to the decision to use structural dampers for vibration mitigation.

To this end, this thesis proposes a new design of a constrained layer damper for reducing the buffeting-induced vibration of HMIPs. The conventional CLD uses a single continuous piece of constraining layer, making it ineffective when applied to circular sections due to the overlapping neutral axes between the constraining layer and the base structure. To overcome this challenge, the proposed CLD has several longitudinal slits added to the constraining layer such that the neutral axes of the slitted constraining layer are separated from the base structure. As a result, the viscoelastic layer is able to develop shear strain under the bending deformation of the base structure, developing viscoelastic damping for vibration mitigation. A series of

comprehensive numerical simulations were performed to: 1) compare the damping capability of different viscoelastic materials; 2) investigate the impact of different CLD parameters on the damping improvement for tubular structures, including the thickness of the viscoelastic layer, the thickness of the constraining layer, and the percentage coverage in the longitudinal direction. The study found that the proposed CLD can increase the damping level of the HMIP to 235% of the inherent damping of the HMIP and reduce its steady-state response at resonance by 57%.

Acknowledgments

I am still on my way to achieving my dreams, yet, earning my master's degree is one big step closer to those. I want to thank everyone who has added joy and growth to my journey so far.

I would like to express my sincere gratitude to my advisor, Professor Jian Li, for his guidance, support, and motivation over the past two years. His enthusiasm for research, deep knowledge, and patience have had a profound impact on me. I am fortunate enough to continue working with him as a Ph.D. student and to have him as my advisor.

I thank Professor Caroline Bennett and Professor William Collins for serving as the thesis committee members and for their insightful comments & recommendations to refine my research. It is always a pleasure to interact with both; their experience has been a great source for me.

I have been fortunate to work with great people from the Department of Civil, Environmental, and Architectural Engineering at the University of Kansas during my master's program. I thank the lab technicians Kent Dye, David Woody, and Carey Meyer for their assistance in preparing for this research field deployment. I also want to thank the Smart Structures and Earthquake Engineering Group members for their thoughtful comments during our group meetings and for helping during the field deployment, which helped keep my research progressing smoothly. I want to thank the Fatigue and Fracture Lab members for their comments and discussions during our weekly meetings and their help whenever I had a question in Abaqus, which improved the content of this thesis.

I thank the Fulbright Program for sponsoring my master's degree at the University of Kansas. I also would like to acknowledge the Kansas Department of Transportation (KDOT) for funding the project.

I realize how fortunate I am to have a family who unconditionally supports me in all my endeavors. I thank my aunts: Khalwa, Maesa, and Asma, for all they have done for me over the course of my life. I thank my siblings, Mai, Ala'a, Hamdi, and Ali, for their encouragement and support during my master's journey. I also thank my friends for our unforgettable memories and adventures during this journey.

Finally, I dedicate this thesis in memory of my parents, Ghadeer and Mudar. Mom and Dad, thank you for raising me, believing in me, and giving me your unconditional love and support. This one is for you.

Table of Contents

List of Figures

List of Tables

Chapter 1: Introduction

High mast illumination poles (HMIPs) are tall, slender structures that vary in length from 100 to 120 ft and are known for having low inherent damping. They are usually found in open areas near highways or rest areas where a high level of illumination is required. As a result, they are vulnerable to excessive vibrations caused by wind loading through various mechanisms, such as vortex shedding, buffeting, and galloping, leading to early fatigue cracks and failures.

The Kansas Department of Transportation (KDOT) discovered premature cracking near the handhole of some HMIPs in Western Kansas. In addition, KDOT captured multiple video recordings of HMIPs having significant vibration under high wind. To investigate the underlying mechanism of such wind-induced vibration in order to guide the selection of vibration mitigation strategies, the recorded videos were analyzed, and a 100-ft tall HMIP near Wakeeney, Kansas, was selected for long-term monitoring using wireless smart sensors. The wireless smart sensor network consists of an anemometer and accelerometers, which were installed at various locations of the HMIP to measure wind speed, wind direction, and wind-induced acceleration responses of the HMIP. Subsequent data analysis revealed that the leading cause of large-amplitude vibrations dominated by the first bending mode was wind buffeting in the along-wind direction due to the fluctuating component of the wind loading. This finding led to identifying structural dampers, rather than aerodynamic dampers, as being appropriate to mitigate the large vibrations of the HMIPs. Subsequently, this thesis proposes and investigates a novel design of a constrained layer damper (CLD) to provide a practical solution to reduce excessive wind-induced vibration of HMIP structures.

Chapter 2 investigates the mechanism of large-amplitude wind-induced vibrations on HMIP structures. A preliminary study was first carried out to analyze the videos from KDOT

using computer vision algorithms. In particular, the Kanade-Lucas-Tomasi (KLT) feature tracking method was applied to detect feature points of the recorded HMIP structure and track the displacement time histories. The power spectral density (PSD) curve of the tracked displacement was then obtained to identify the dominant frequency of the vibration. An FE model was built to confirm that vibration was dominated by the first bending mode of the structure. Subsequently, a wireless smart sensor network based on the Xnode smart sensor platform (Fu et al., 2018) was designed to perform long-term monitoring of a 100-ft tall HMIP located in Wakeeney, KS. The sensor network was designed to measure the vibration amplitude through accelerometers, and wind speed and direction were measured using an anemometer. The obtained acceleration and wind measurements were then utilized to determine the nature of wind-induced vibration.

Chapter 3 numerically investigates the mitigation of buffeting-induced vibration for HMIPS. This chapter proposes a novel CLD design to increase the structural damping of the HMIP structure. The CLD consists of a viscoelastic material confined between the base structure and the constraining layer. It absorbs vibration energy by hysteresis via shear strain in the viscoelastic material when the structure vibrates in bending. Traditional CLD design uses a single piece of constraining layer, which becomes ineffective when applied over circular cross-sections due to the overlapping neutral axes between the constraining layer and the base structure. The proposed CLD design adds longitudinal slits to the constraining layer to break the constraining layer into multiple independent strips, effectively separating the neutral axes from the base layer. A series of comprehensive numerical analyses are carried out in this chapter to investigate the performance of the CLD under the influence of several factors, such as the viscoelastic material thickness, constraining layer thickness, and longitudinal percent coverage.

Chapter 4 summarizes the findings and conclusions from Chapter 2 and Chapter 3 and discusses the future work.

Chapter 2: Wind-induced Vibration Monitoring of High Mast Illumination Poles

Abstract

This chapter describes the use of wireless smart sensors for examining the underlying mechanism for the wind-induced vibration of high mast illumination poles (HMIP) structures. HMIPs are tall, slender structures with low inherent damping. Video recordings of multiple HMIPs showed considerable vibrations of these light poles under wind loading in the State of Kansas. Cyclic large-amplitude displacements can produce high-stress demand at the pole base and lead to fatigue cracking. In this study, the fundamental natural frequencies of the HMIP were assessed using finite element modeling, and the recorded vibration frequencies were obtained through computer vision based video analysis. Meanwhile, a 100-ft-tall HMIP with three LED luminaires made of galvanized steel located in Wakeeney, Kansas, was selected for long-term vibration monitoring to investigate the underlying reason for the excessive wind-induced vibrations.

2.1 Introduction

High mast illumination poles (HMIPs) are tall, slender structures that vary in length from 100 ft to 120 ft. They are usually found in open areas near highways or rest areas where a high level of illumination is required. These structures are known for having low inherent damping. They are susceptible to excessive vibrations due to wind loading through various vibration mechanisms such as vortex shedding, buffeting, and galloping, which can lead to premature fatigue cracking in the HMIPs.

Vortex shedding occurs due to negative pressure caused by alternating wind vortices on the side of the structure, causing the structure to oscillate in the direction perpendicular to the

wind (Zuo et al., 2008). When the frequency of vortex-induced vibration (VIV) matches the structure's natural frequency, a "lock-in" phenomenon occurs. VIV induced lock-in typically happens at higher modes, such as the second or third mode (Puckett et al., 2010). On the other hand, buffeting is excited by wind turbulence caused by wind gusts resulting in vibration response with multiple modes (Chen et al., 2015). The amplitude of this type of vibration is known to increase with the increase in wind speed (Zuo et al., 2008), causing the structure to experience large displacements (Zuo et al., 2008). Buffeting-induced vibration is forced vibration in the direction of the wind (Caracoglia et al., 2007). Galloping-induced vibration is featured by large amplitude and unstable aerodynamic vibration, which usually occurs in the cross-wind direction (Zuo et al., 2008). Galloping is influenced by the lift and drag coefficients of the structure, as well as the wind attack angle. Because the lift and drag coefficients for a circular section are constant, galloping vibration is unlikely to occur in HMIPs with circular sections unless rain or snow adheres to the structure's surface, changing its circumferential characteristics (Caracoglia et al., 2007).

In the United States, HMIPs are designed according to "AASHTO Standard Specifications for Structural Supports for Highway Signs, Luminaires and Traffic Signals" (AASHTO, 2015) to withstand different loads, including wind loads. However, the wind loading described by these specifications is mainly based on wind tunnel testing, which may not fully reveal the wind excitation mechanism (Zuo et al., 2008). Studies have shown that long-term wind-induced vibrations on these poles in high-stress areas can create cumulative fatigue damage, cracks, and potential failure (Li-Wei Tsai et al., 2020). This chapter investigates the reason and mechanism behind the excessive wind vibration of HMIP structures through finite element modeling, video analyses, as well as long-term field monitoring and data analysis.

2.2 Methodology

The fundamental natural frequencies and the recorded vibration frequencies of the HMIP were assessed using finite element modeling and video analysis, respectively. To determine the source of the HMIP's vibration, a preliminary study on several recorded videos of vibrating HMIPs was carried out through video analysis using the Kanade-Lucas-Tomasi (KLT) feature tracking approach to extract the maximum displacement and the vibration frequencies of the structure. Meanwhile, a 100-ft-tall HMIP with three LED luminaires made of galvanized steel was selected for long-term vibration monitoring. By collecting acceleration responses and wind velocity and direction data over a three-month period, extensive data analysis was performed to characterize the nature of wind-induced HMIP vibrations in order to uncover the reason behind the vibrations with excessive amplitudes. In addition to long-term monitoring, pluck tests were also performed to determine the inherent damping ratio of the HMIP.

2.3 Preliminary Investigation

Several video recordings of vibrating HMIPs captured by the Kansas Department of Transportation (KDOT) were analyzed using the KLT method to extract the vibration frequencies. As illustrated in Figure 2-1 (a), the top of the pole where the maximum displacement occurs was picked as the region of interest. The displacement of the HMIP was then tracked using the KLT feature point tracker, which was used to estimate the natural frequency of the light pole (Almarshad, 2020). Results indicated that the average tracked displacement was approximately 12 in., as shown in Figure 2-2 (a). Then the power spectral density (PSD) of the tracked displacement showed that a mode with a natural frequency equal to 0.61 Hz dominated the vibration, as illustrated in Figure 2-2 (b). Following the observation of significant vibrations and the preliminary video-based modal analysis, FE modeling, monitoring,

and data analysis were conducted to further investigate the causes of the HMIP's vibrations. It should be noted that the monitored HMIP is not identical to the ones seen in the videos, but they do share similar characteristics such as material properties, height, slenderness ratio, and similar natural frequencies, which make it a good fit for the preliminary study.

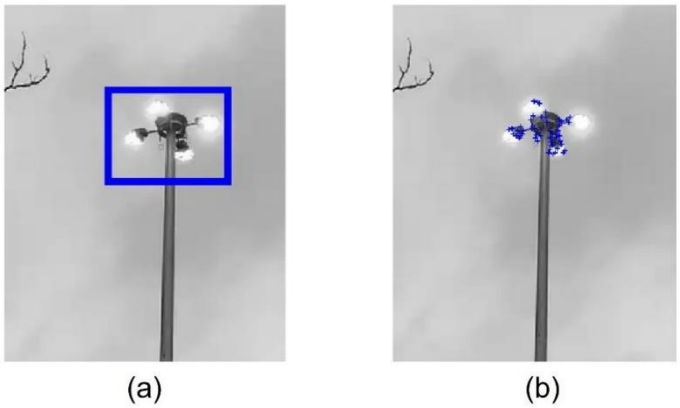

Figure 2-1 (a) Region of interest for displacement tracking; (b) Detected feature points used in the tracking

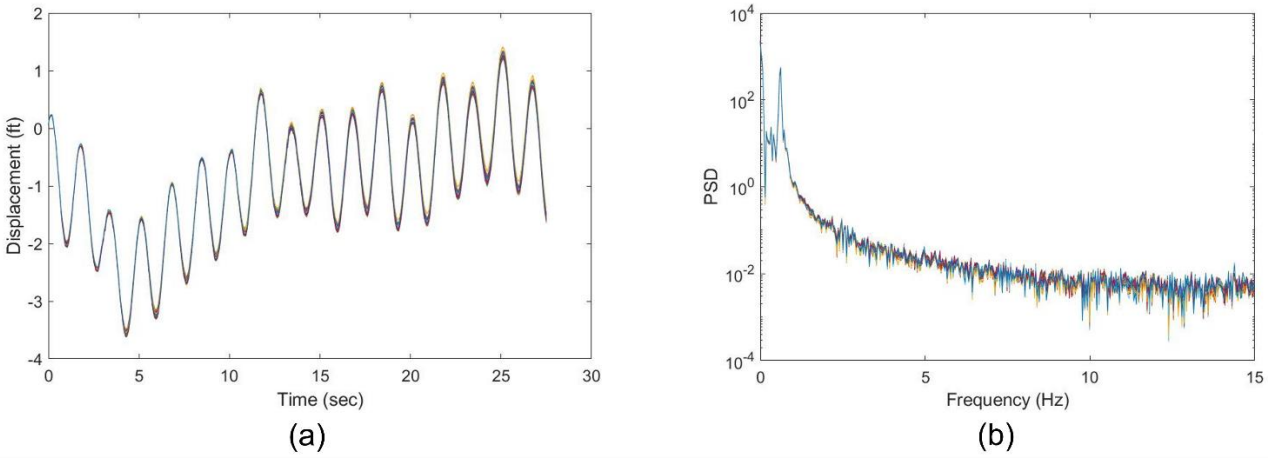

Figure 2-2 (a) Displacement time history of the top of the HMIP tracked by the KLT method; (b) Power spectral density of the tracked displacement

2.4 Long-Term Field Monitoring

2.4.1 Location and Geometry of the Selected HMIP

A 100-ft-tall HMIP located in an open highway rest area in Wakeeney, Kansas, was selected for field monitoring, as shown in Figure 2-3. The HMIP structure has a 0.33-degree tapered circular section and is made of galvanized steel. As illustrated in Figure 2-4, it consists of two discrete sections with different heights, and Table 2-1 summarizes the dimensions of the selected HMIP. According to the design, a minimum of 28.31 in. overlap is required by the Kansas Department of Transportation (KDOT), as demonstrated in Figure 2-5. However, the manufacturer did not define the exact overlap between sections A and B; later, it was estimated to be 41.25 in. by determining the height at which the outer diameter of part A matches the base inner diameter of part B.

A light assembly is located at the top of the pole, which weighs 406 lb and consists of three LED light fixtures and a lowering device. The HMIP has a handhole that is 12.25 in. wide and 32 in. tall and is located 28.75 in. above the base plate, as depicted in Figure 2-6. The handhole allows access to operate the lowering device and carry out maintenance of the HMIP.

Figure 2-3 The selected HMIP located in Wakeeney, Kansas, for long-term monitoring

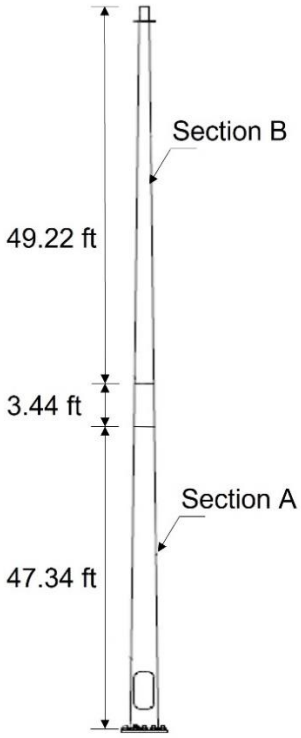

Figure 2-4 Schematic of the HMIP

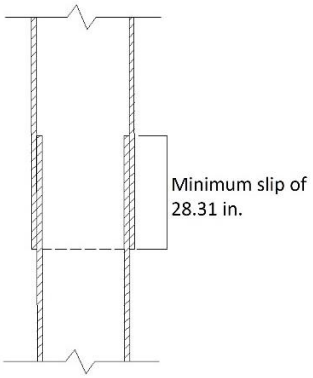

Figure 2-5 Slip joint details

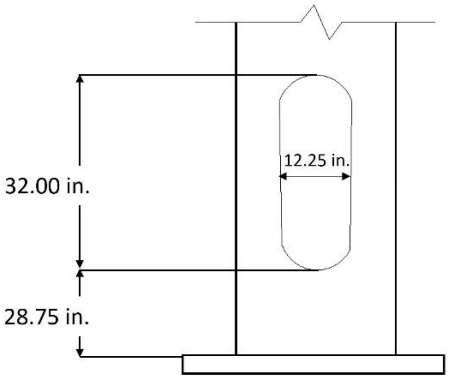

Figure 2-6 Handhole details

Table 2-1 Dimensions of the HMIP cross-sections

	Base Diameter (in.)	**Top Diameter (in.)**	**Length (ft)**	**Thickness (in.)**
Section A	25.50	18.39	50.80	0.250
Section B	19.25	11.87	52.68	0.188

2.4.2 Wireless Smart Sensor Network

A wireless smart sensor network was designed for long-term field monitoring using Xnodes from Embedor Technologies (Fu et al., 2018), as shown in Figure 2-7. The wireless smart sensor network consists of three remote sensor nodes and one gateway sensor node; each of them is equipped with triaxial accelerometers. One of the remote sensor nodes was connected to an M. Young propeller vane anemometer (Model 05103V), as illustrated in Figure 2-8, through a breakout box to measure the wind speed and direction. The sensor nodes are powered by rechargeable batteries and solar panels, and the anemometer was powered using a 12 V battery connected to a solar panel. The sensitivity of the wind speed output of the anemometer is 50 mV per m/sec, and the sensitivity of wind direction output is 13.9 mV per degree (R. M. Young Company, 2000). The sensor nodes spend most of the time in deep sleep mode to conserve energy and can be triggered to wake up immediately for data collection through an on-board low-power accelerometer which constantly monitors ambient vibration level. An acceleration threshold which is programmable is stored in each sensor node for triggering data collection for the sensor nodes under large vibration. Since each sensor node is triggered independently, the data collected by the sensor nodes are not synchronized. The gateway sensor node communicates with the other three remote sensor nodes to collect their data and upload it to the cloud using a 4G cellular network. The cloud server and database can be accessed from a website where data can be visualized and downloaded. The website also provides the interface to remotely change parameters of the sensor networks, such as the triggering threshold.

The sensors were installed on the HMIP at different heights, as shown in Figure 2-9, which was determined based on the HMIP's mode shapes obtained from an FE model, such that the sensor captured vibrations from multiple modes. The cellular gateway node was placed at the

lowest elevation where the vibrations are minimized, so it will be triggered less often to ensure reliable communication with the remote sensors and upload the data. The anemometer was installed at the height of 77 ft and connected to the Xnode located at the same height. A 4-ft-long bracket support was used to support the anemometer to reduce the impact of wind turbulence for reliable wind measurements. Note that the recommended support length is six times the HMIP diameter to minimize upstream and downstream flow distortions (Barthelmie et al., 2016). However, for practical reasons, the support length adopted in the bracket was 3.2 times the HMIP diameter. In this investigation, the direction of vibration in relation to wind direction is critical to determine the main reason behind the excessive wind vibration. The orientation of the sensors with the light assembly is shown in Figure 2-10. As illustrated in Figure 2-11, the sensor nodes are oriented in the northeast direction. The Z-axis of the sensor nodes is angled 25 degrees to the east and aligned with the anemometer's 0-degree angle.

Figure 2-7 Xnode wireless sensor and solar panel

Figure 2-8 Anemometer and the bracket support

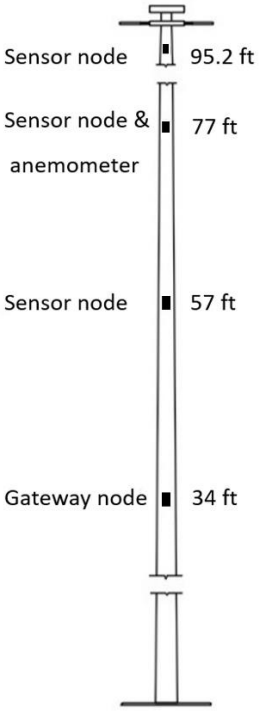

Figure 2-9 Locations of the deployed wireless sensors along the HMIP

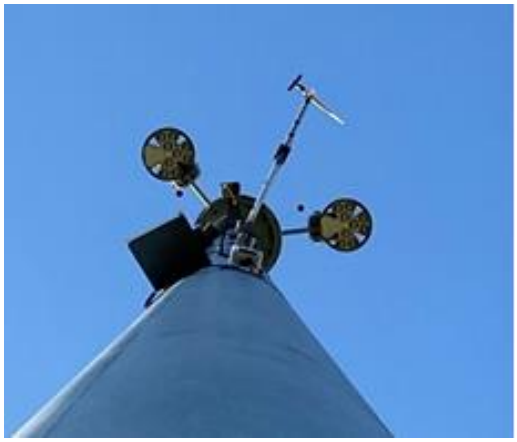

Figure 2-10 The alignment of the sensors and the luminaries

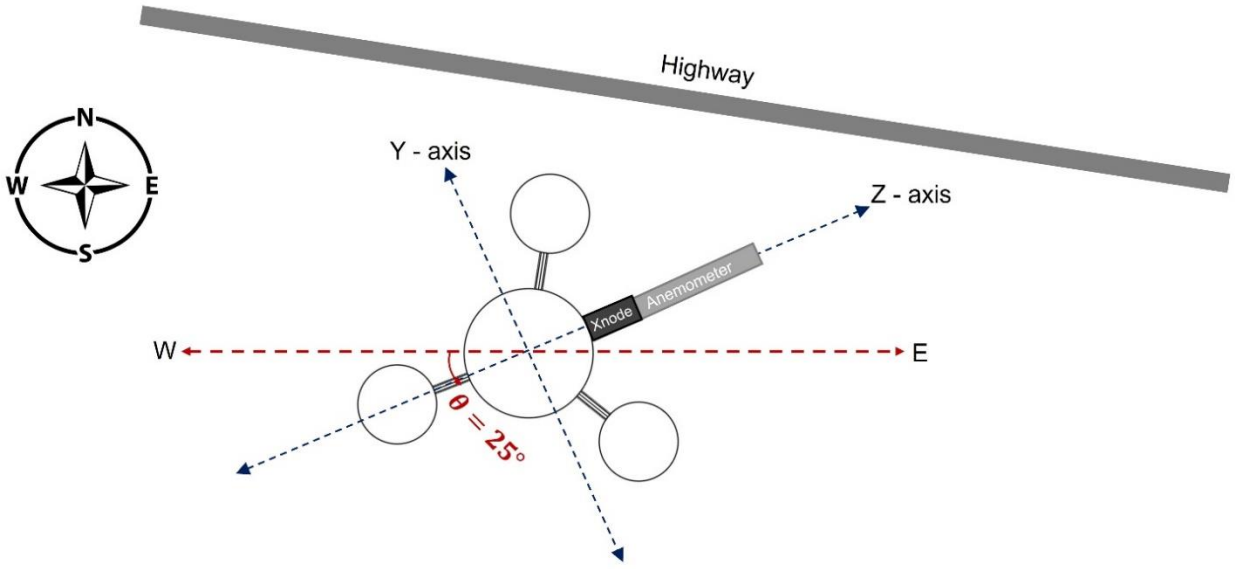

Figure 2-11 Illustration of sensor orientations

2.5 Pluck Test

Pluck tests were performed after instrumenting the HMIP to determine the inherent damping ratio of the first mode of the monitored HMIP. The test was conducted by attaching a steel wire cable to the HMIP at the height of 50 ft, then connecting it to a quick-release shackle attached to a pickup truck equipped with a come-along winch and a load scale, as shown in Figure 2-12.

An initial displacement was applied to the HMIP by pulling the cable using the come-along winch and then releasing it with the quick-release shackle to let the HMIP vibrate freely. In the meantime, the sensor network was triggered to collect the acceleration response under free vibration. To estimate the damping ratio using the measured free vibration response from the pluck test, the measured acceleration data obtained from the sensor at the height of 95.5 ft were first filtered using a low-pass elliptic filter with a cut-off frequency of 1.8 Hz to remove frequencies above the first natural frequency. From the filtered free decay response, the damping ratio can be estimated using the logarithmic decrement (δ) method based on two peak amplitudes separated by *N* cycles, in which δ is given by:

$$\delta = ln\left(\frac{U_P}{U_Q}\right) = \zeta\omega_n T_d N = \frac{2\pi N\zeta}{\sqrt{1-\zeta^2}} \tag{2-1}$$

where U_P is the peak amplitude of the first cycle, U_Q is the peak magnitude of the (N+1)th cycle. T_d is the damped natural period, which is equal to $\frac{2\pi}{\omega_d} = \frac{2\pi}{\omega_n\sqrt{1-\zeta^2}}$. For a small damping ratio, $\sqrt{1-\zeta^2} \approx 1$. Thus, the damping ratio can be approximated as:

$$\zeta = \frac{1}{2\pi N} ln\left(\frac{U_P}{U_Q}\right) \tag{2-2}$$

Subsequently, the first mode damping ratio was estimated to be around 0.8% using the logarithmic decrement method given in Equation (2-2). Figure 2-13 presents a verification of the estimated damping ratio by showing the filtered free vibration response from the pluck test and its envelope curve associated with a 0.8% damping ratio.

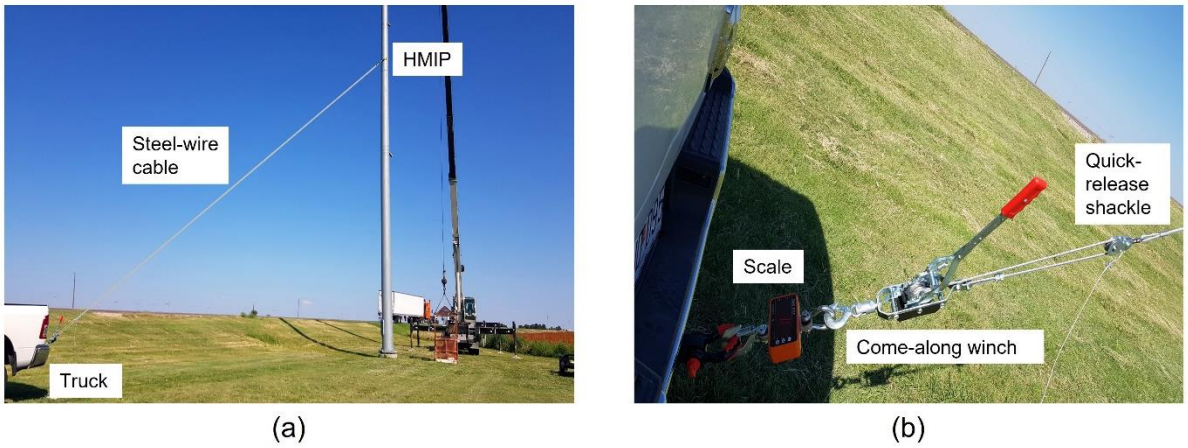

Figure 2-12 (a) Illustration of the pluck tests; (b) Tools used in the pluck tests

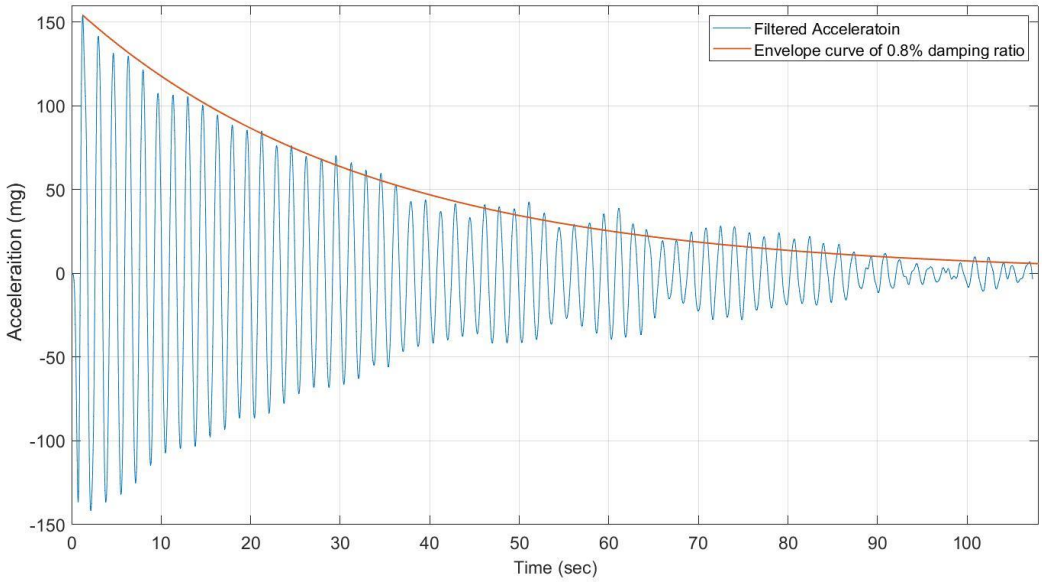

Figure 2-13 Low-pass filtered free vibration response at the height of 95.2 ft from the pluck test

2.6 Data from Long-Term Vibration Monitoring

The HMIP was monitored for three months, from September 18, 2021, to December 28, 2021. Figure 2-14 presents a summary of the collected data in terms of date and time. During the monitoring period, 1102 datasets were collected. The data were sampled at 50 Hz. The triggering threshold was initially set at 70 mg for the first month to assess the vibration level of the HMIP under wind load, then it was raised to 300 mg to limit data collection for only significant wind events. As a result, as shown in Figure 2-14, more datasets were collected during the first month, and only significant wind events were recorded during the other two months. The gap in the collected data after October 16, 2021, is attributed to the sensors losing battery charge due to some excessive wind vibration that kept triggering the sensors on cloudy days, during which the solar panels could not recharge the batteries.

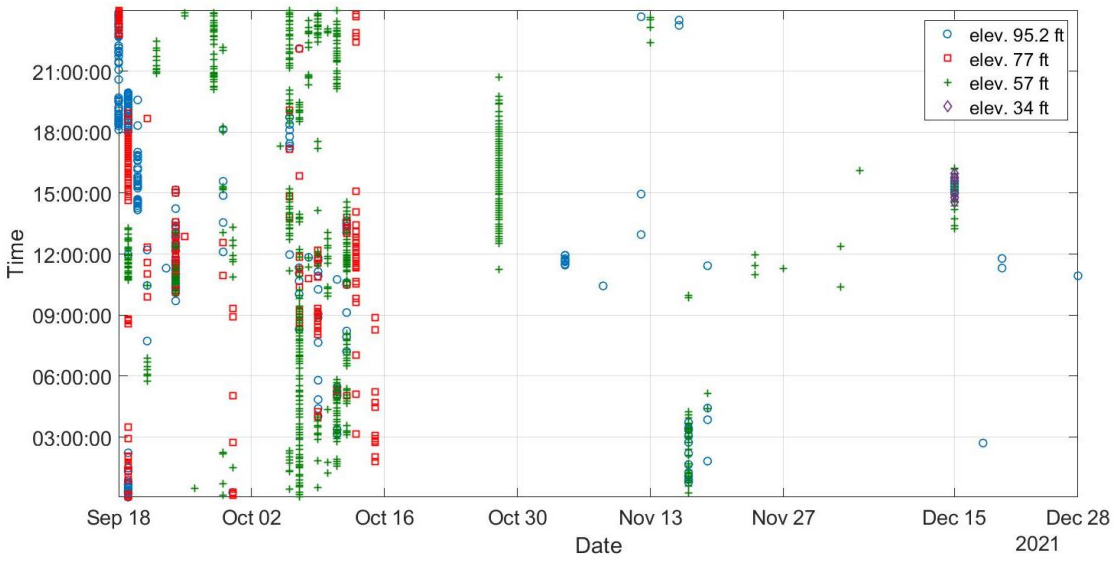

Figure 2-14 Overview of data collected over the three-month monitoring period

2.6.1 Identified and Analytical Modal Properties

The natural frequencies of the HMIP were identified using the PSD functions obtained from the collected acceleration data, which were validated by a preliminary FE model based on

the detailed drawings and design documents of the HMIP. The first three natural frequencies in the y-direction were determined to be 0.61 Hz, 2.73 Hz, and 7.48 Hz, respectively. Additionally, the first three natural frequencies in the z-direction were identified as 0.60 Hz, 2.68 Hz, and 7.32 Hz, respectively. The slight difference in natural frequencies in the y and z directions could be attributed to signal processing uncertainties and possible asymmetry in the structure.

An FE model of the HMIP was created based on the design drawing using an eight-node linear brick element (C3D8) in Abaqus CEA, version 6.24 (ABAQUS, 2021). The HMIP was modeled as two tapered segments with a lumped mass at the top, which corresponds to the light assembly and lowering device. Figure 2-15 (b) illustrates the first three analytical mode shapes of the modeled HMIP, and the corresponding natural frequencies are 0.65 Hz, 2.88 Hz, and 7.69 Hz, respectively. Table 2-2 summarizes the analytical natural frequencies obtained from the FE model and those identified from the wind-induced vibration measurements. As mentioned previously, the mode shapes were not obtained from the field monitoring because the sensors were triggered independently; hence, the measured acceleration responses were not synchronized.

Table 2-2 Analytical and identified natural frequencies of the HMIP

	First mode	**Second mode**	**Third mode**
FE model	0.65 Hz	2.88 Hz	7.69 Hz
Wind-induced vibration (Y direction)	0.61 Hz	2.73 Hz	7.48 Hz
Wind-induced vibration (Z direction)	0.60 Hz	2.68 Hz	7.32 Hz

Note Table 2-2 from Shaheen et al. (2022)

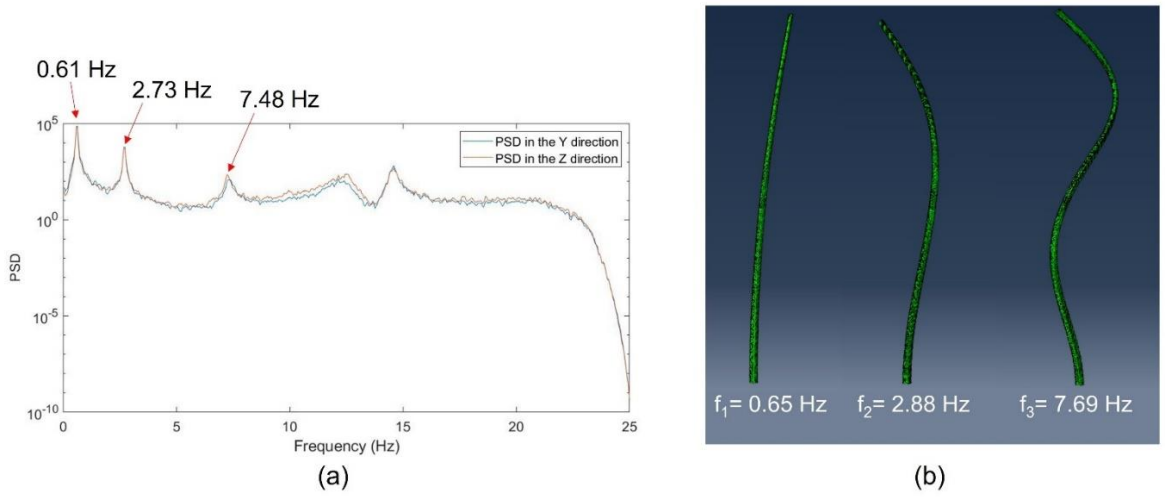

Figure 2-15 (a) Natural frequencies from wind-induced vibration; (b) Natural frequencies and mode shapes from the FE model

2.6.2 Data Analysis

This study aims to assess the cause of excessive vibration of the HMIP structure based on the monitored acceleration and wind (velocity and direction) data collected by the wireless smart sensor network. Previous studies on light pole structures distinguished the mechanism behind the excessive wind vibration by identifying the natural frequencies and modes involved in the vibration and determining the alignment of the light pole's vibration direction with the wind direction. For instance, Puckett et al. (2010) monitored a 120-ft HMIP and found that it experienced third mode lock-in due to vortex shedding at wind speeds between 10 mph to 19 mph, for which the vibration occurred in the cross-wind direction. Zuo et al. (2008) monitored a 40-ft cantilevered light pole and found that vortex-induced vibrations experienced by the light pole were dominated by the second mode under specific wind speed ranges, with the vibration perpendicular to the wind direction. In addition, buffeting-induced vibrations which occurred in the along-wind direction were dominated by the first mode, and they showed large unsteady vibration amplitudes, which increased when wind speed increased.

During data analysis, the characteristics of the triggered acceleration data from wind loading were investigated. The acceleration time history for the collected buffeting-induced vibration exhibited amplitude fluctuation according to the wind speed, as illustrated in Figure 2-16. Additionally, buffeting-induced vibration showed multiple modes involved in the HMIP vibration, with the first mode having the highest amplitude in PSD, as shown in Figure 2-18 (a). Meanwhile, Figure 2-17 (a) shows the VIV-governed acceleration time history, in which the HMIP is shown engaged in VIV for the first 60 seconds. The captured VIV acceleration time history is periodic with a single frequency component. VIV is featured by a lock-in phenomenon when the vortex shedding frequency matches the natural frequency of the HMIP. As a result, only one mode will be visible in the PSD curve. Figure 2-18 (b) shows a second mode lock-in caused by vortex shedding on the HMIP.

The acceleration data was converted to displacement using a time-domain Finite Impulse Response (FIR) filter that eliminates low-frequency drift caused by double integration. A detailed description of this method can be found in (Almarshad et al., 2019; Park et al., 2013). The displacement's magnitude was calculated using the square root of the sum of squares (SRSS) of the collected displacement in the Y and Z axes for each data set, and the angle of the magnitude demonstrates the direction of the HMIP vibration.

The alignment of the HMIP vibration relative to the wind direction was assessed to determine if the vibration was in the along-wind or cross-wind direction. Therefore, the normalized displacement's magnitude and direction were plotted alongside the normalized wind rose from the collected wind speed and direction, as shown in Figure 2-20 (b). The figure shows that the wind direction is consistent with the HMIP's vibration direction; hence it belongs to along-wind vibration. Note that this type of vibration is represented by most of the collected

data, as will be discussed later. The slight difference in the anemometer and Xnode data can be attributed to a minor misalignment between the sensors and the anemometer.

For further data analysis, Figure 2-19 shows the displacement amplitude of each collected dataset along with the associated number of modes. As concluded by previous analysis, datasets that contain more than one mode are categorized as buffeting-induced vibrations, and the ones that contain a single mode are categorized as VIV. It can be noted that the multimode vibration occurred more frequently than the single mode. In addition, the displacement amplitudes of multimode vibrations are significantly higher than ones with single mode, indicating that buffeting-induced vibration is likely the primary source of the observed excessive vibrations.

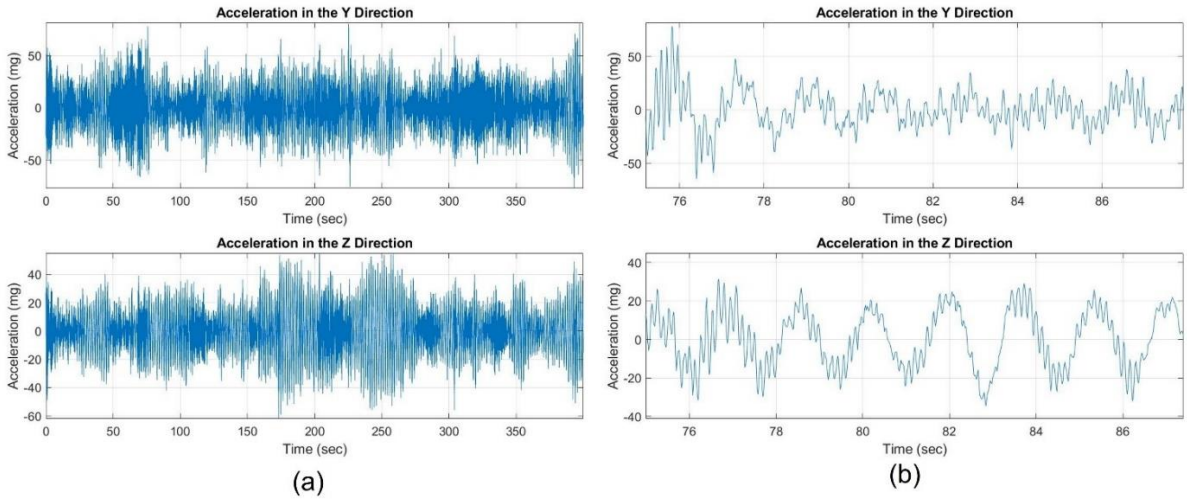

Figure 2-16 Acceleration time histories of buffeting-induced vibration; (b) Detailed acceleration time histories

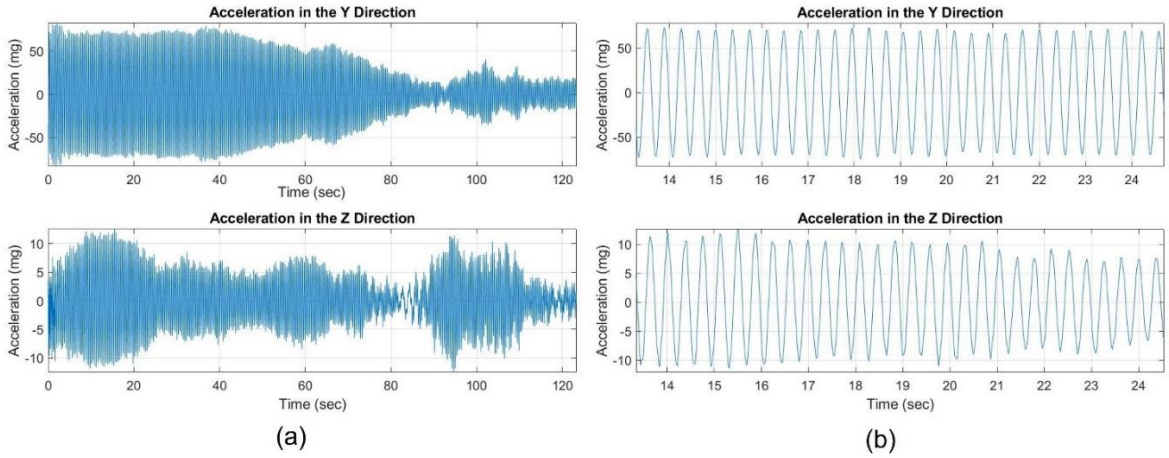

Figure 2-17 Acceleration time histories associated with VIV; (b) Detailed acceleration time histories

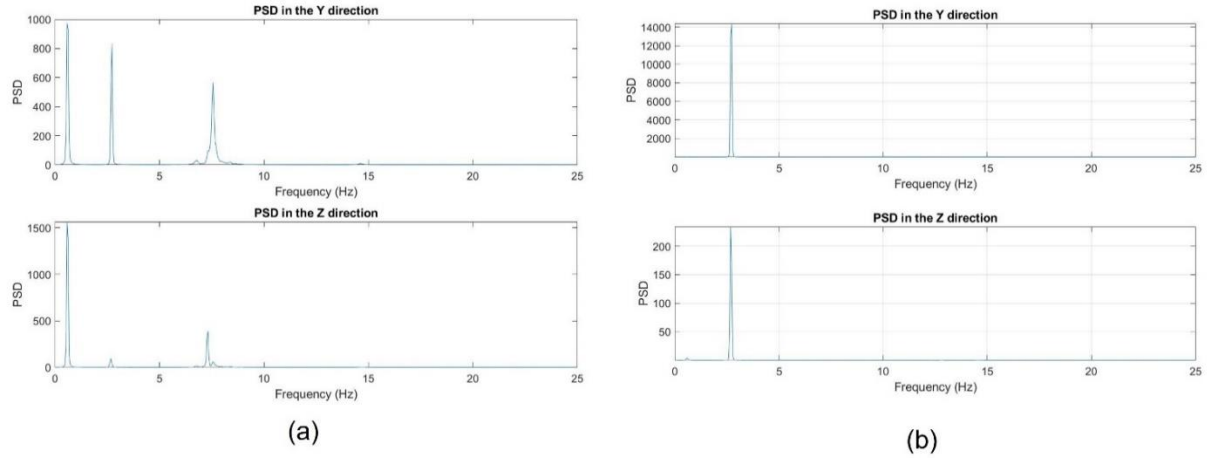

Figure 2-18 PSD curves for buffeting-induced vibration; (b) PSD curves for VIV

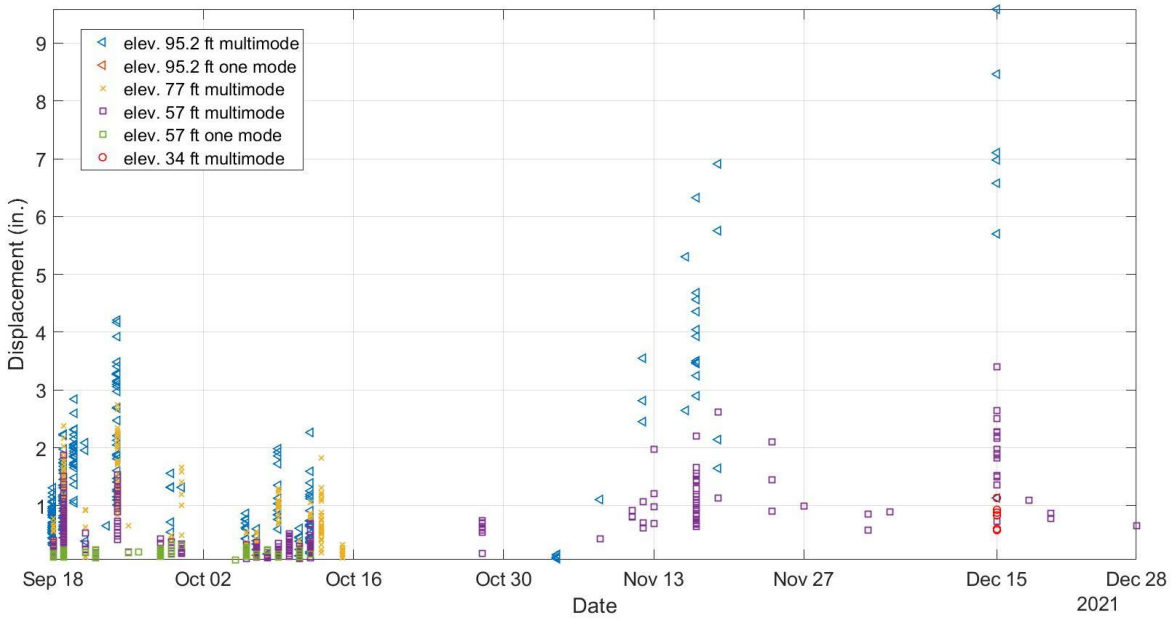

Figure 2-19 Overview of the number of triggered modes and displacement amplitude from the collected data

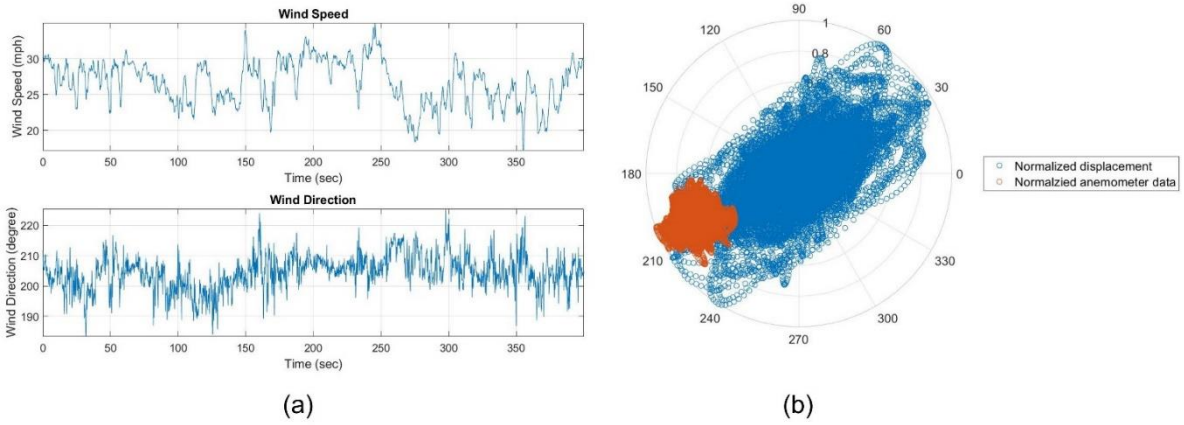

Figure 2-20 (a) Collected wind speed and wind direction; (b) Normalized wind rose to the maximum value

The highest displacement amplitude during the long-term vibration monitoring period was captured on December 15, 2021, when a Derecho storm occurred, as shown in Figure 2-21. This type of storm is known for its high wind speed and large wind gusts. According to a nearby weather station, the maximum recorded wind speed on that day was 58 mph, and the maximum

wind gust reached 84 mph (Hays Regional Station, 2021). On that day, the wireless smart sensor connected to the anemometer lost connection with the gateway node; hence the wind data was unavailable. However, since the anemometer's wind direction data previously matched the weather station's data, the study of the excessive wind vibration on that day is based on the weather station and data from the sensor installed at the height of 95.2 ft.

As illustrated in Figure 2-21, the amplitude of the displacement time history during the storm fluctuated with the wind speed and reached large amplitudes. The maximum recorded total displacement magnitude was about 9.5 in., as shown in Figure 2-22, which is the closest to the 12 in. displacement captured in the video from KDOT. In addition, the first mode dominated the vibration, with several other modes involved in exciting the HMIP, as illustrated in Figure 2-23 in both linear and log scales. To assess the alignment of the vibration's direction with the wind direction, the normalized displacement magnitude and direction were plotted in Figure 2-24. In addition, according to the nearby weather station, the wind direction during the storm was West-Southwest (WSW) (Hays Regional Station, 2021), indicating that the vibration direction was in the along-wind direction. Hence, the excessive wind vibration during the derecho storm exhibited the characteristics of buffeting-induced vibration in terms of the large amplitude, multi-mode, and along-wind vibrations.

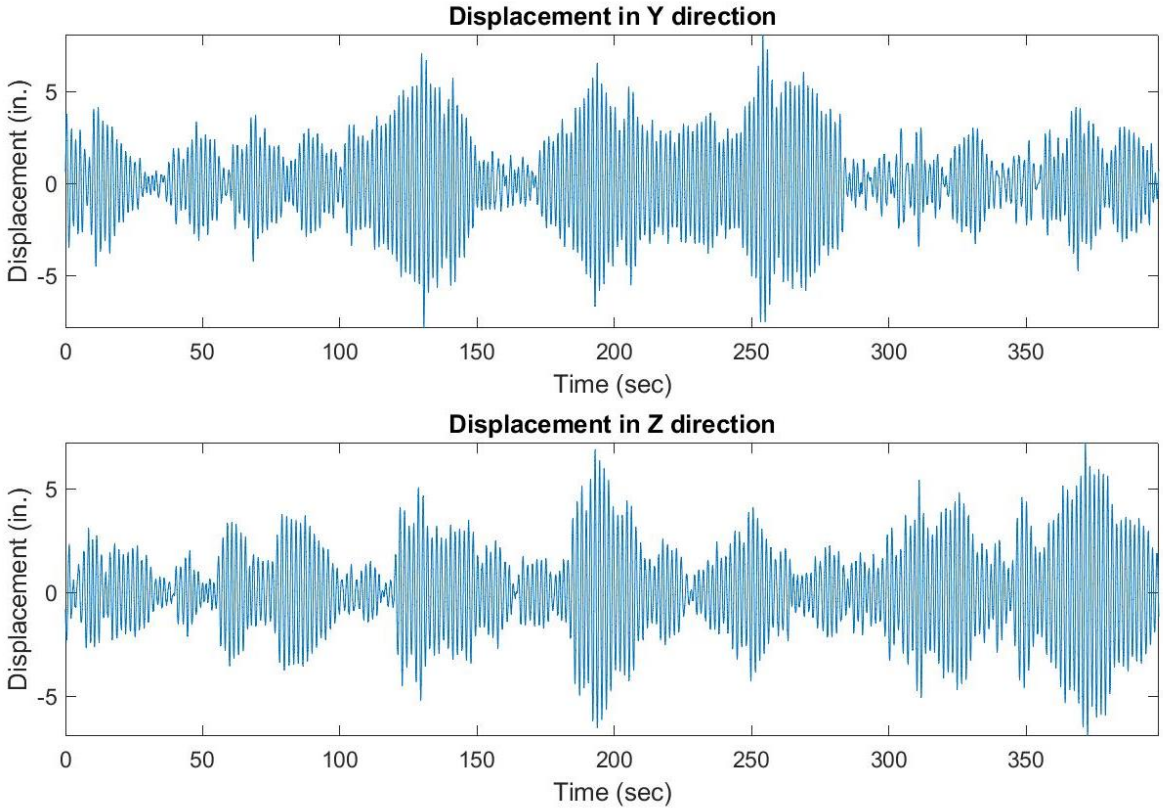

Figure 2-21 Displacement time history during the derecho storm

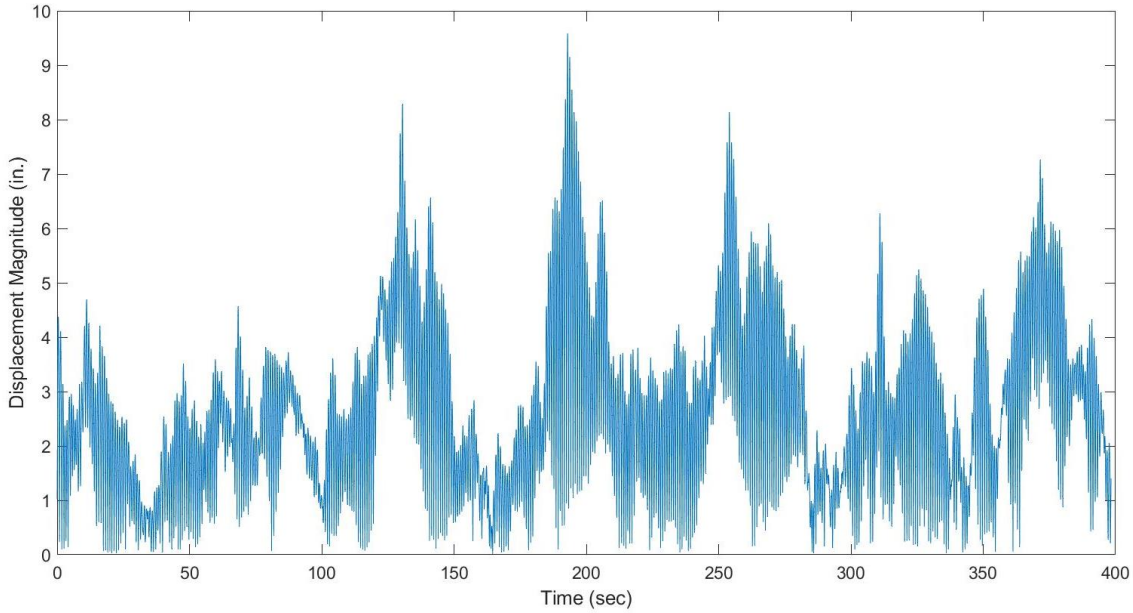

Figure 2-22 Time history of total displacement magnitude measured from the derecho storm

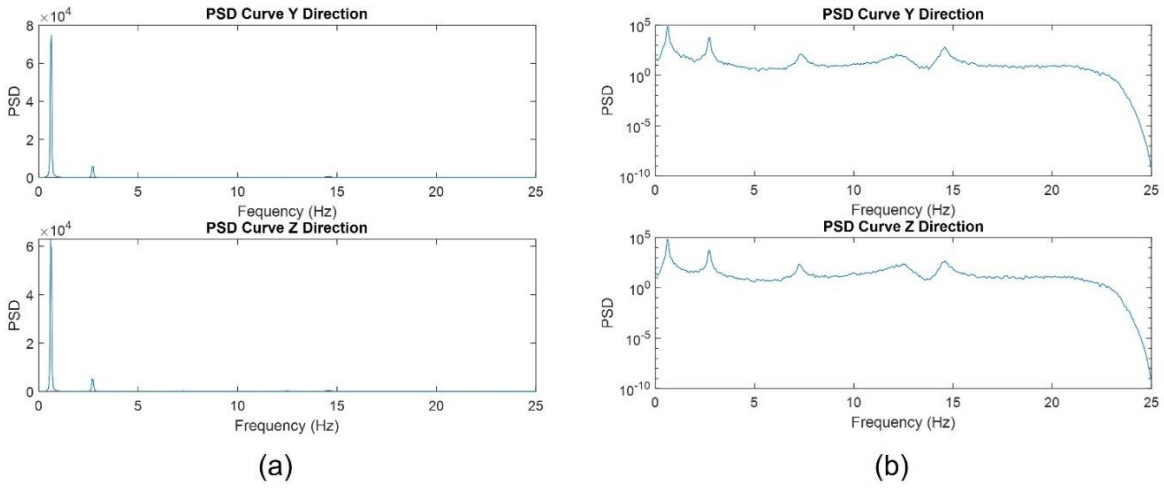

Figure 2-23 PSD of acceleration responses measured during the Derecho storm (a) linear scale; (b) log scale

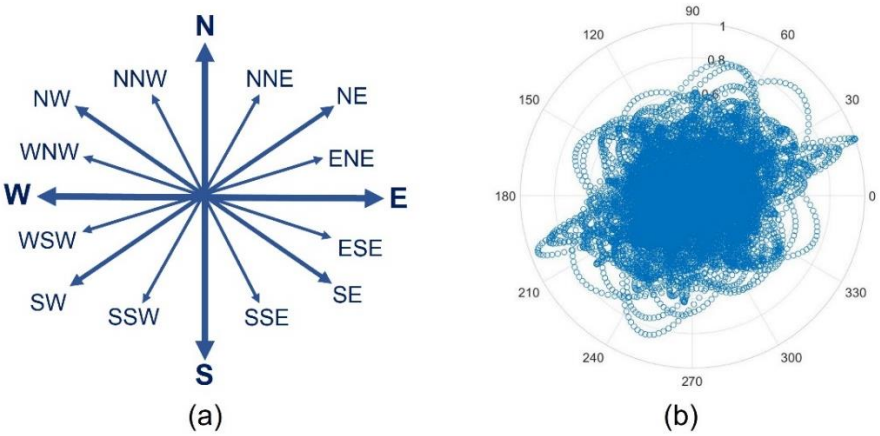

Figure 2-24 (a) Cardinal coordinates; (b) Normalized displacement measured during the derecho storm

2.7 Conclusions

This study examined the mechanism of the excessive wind-induced vibrations on a 100-foot-tall HMIP in Wakeeney, Kansas. First, video analysis of multiple recordings captured by KDOT was performed using the KLT feature tracking approach to extract the structure's maximum displacement and vibration frequencies. In addition, a three-month monitoring was conducted to collect acceleration responses and wind speed and direction data to understand the main reason behind the HMIP's vibrations that exhibit excessive amplitudes.

The video analysis indicated that the structure's vibration is dominated by a 0.61 Hz mode, with a maximum displacement of 12 in., which was confirmed as the first-mode vibration through FE analysis. From the long-term field monitoring, it was found that the HMIP experienced two types of wind-induced vibrations. The first one is called buffeting-induced vibration, which occurs in the along-wind direction. The second type is called vortex-induced vibration (VIV), which occurs in the cross-wind direction. Buffeting-induced vibrations are excited by the turbulence component of wind load, thus, often include multiple frequency components and are typically dominated by the first mode. On the other hand, VIV is caused by the steady vortex shedding, which excites the structure in the cross-wind direction. The monitored HMIP structure demonstrated second-mode lock-in under VIV. During the field monitoring, buffeting-induced vibration occurred more often than VIV and had greater amplitudes. In particular, the maximum displacement recorded at the top of the HMIP was 9.5 in. during a derecho storm, demonstrating that vibration caused by buffeting can produce large displacements at the top of the structures and hence high-stress demand at the bottom. Therefore, further investigation on vibration mitigation strategies should focus on vibrations induced by buffeting.

Chapter 3: Numerical Investigation of Constrained Layer Damper to Reduce Buffeting-induced Vibration of HMIPs

Abstract

This chapter proposes a new design of a constrained layer damper for reducing the buffeting-induced vibration of HMIPs. The conventional CLD uses a continuous constraining layer, making it ineffective when applied to circular sections due to the overlapping neutral axes between the constraining layer and the base structure. To overcome this challenge, the proposed CLD has several longitudinal slits added to the constraining layer such that the neutral axes of the slitted constraining layer are separated from the base structure. As a result, the viscoelastic layer is able to develop shear strain during bending deformation of the base structure, developing viscoelastic damping for vibration mitigation. A series of comprehensive numerical simulations were performed to: 1) compare the damping capability of different viscoelastic materials and 2) investigate the impact of different CLD parameters on the damping improvement for tubular structures, including the thickness of the viscoelastic layer, the thickness of the constraining layer, and the percentage coverage in the longitudinal direction. The study found that the proposed CLD can increase the damping level of the HMIP to 235% of the inherent damping of the HMIP and reduce its steady-state response at resonance by 57%.

3.1 Introduction

High mast illumination poles (HMIPs) are tall, slender structures usually installed on highways where high illumination is needed. The HMIPs system comprises a light assembly and a lowering device mounted on a flexible cantilever, typically 100 to 120 feet tall. Despite their simple design and compliance with the code, these HMIPs are known to have low inherent damping, and some have previously experienced fatigue cracks and failed due to excessive

vibrations under the wind. The failure of these HMIPs imposes a high risk of wind-induced hazard due to their locations. Therefore, various vibration mitigation strategies have been investigated to reduce the excessive vibrations of these HMIPs depending on the mechanism behind the vibrations.

A study conducted by the University of Kansas on a 100-ft tall HMIP located in Wakeeney, Ks, found that the HMIP is susceptible to large amplitude vibrations due to wind-induced buffeting, as discussed in Chapter 2. This chapter investigates a vibration mitigation device to reduce buffeting-induced vibration on HMIP structures.

3.1.1 Literature Review

Aerodynamic and structural dampers have been used to reduce wind-induced vibrations on slender light poles, depending on the cause of the vibration. Aerodynamic dampers modify the surface and geometry of the original structure. As a result, they alter the aerodynamic properties of the system and disturb the formation of vortices. Hence, this type of damper can be used to dampen vibration caused by vortex shedding. For example, aerodynamic dampers such as ribbon retrofit, helical strakes, perforated shrouds, and surface roughness were investigated and installed on a 120-feet-tall HMIP in Wyoming to reduce vortex-induced vibration (VIV) (Puckett et al., 2010). These aerodynamic dampers were chosen to retrofit the HMIP because they do not interfere with the HMIP's lowering device, are cost-effective, and are easy to install (Puckett et al., 2010). From the study, the perforated shrouds effectively avoided the third mode lock-in among the four installed aerodynamic dampers (Puckett et al., 2010).

Structural dampers, on the other hand, function differently than aerodynamic dampers, as they reduce vibration by increasing the damping capability of the structure. Various structural dampers have been installed on light poles, such as tuned mass dampers, Stockbridge dampers,

and impact dampers. The tuned-mass damper is designed to vibrate at specific natural frequencies of the system and is usually installed on high-rise buildings and slender towers. When the structure oscillates, the tuned-mass damper is excited and vibrates in opposition to the magnitude of the structure's vibration (Puckett et al., 2010); consequently, it reduces unwanted vibrations. A Stockbridge damper has two masses attached at the end of a flexible shaft and can be installed inside or outside the structure. The Stockbridge damper is generally designed at a frequency close to the structure's second or third natural frequency, preventing lock-in (Kaczinski et al., 1998). The Stockbridge dampers were installed on the exterior of existing light poles in New Jersey and effectively reduced VIV (Kaczinski et al., 1998).

Impact dampers come in various types, including ball impact damper, tube damper, rod in a canister damper, and chain damper. They can be used to reduce vortex or buffeting-induced vibration. Impact dampers dissipate energy through exchanging momentum and collision impact. Impact dampers can be modeled as a spring with viscous damping (Li et al., 2009). The ball impact damper is a freely moving mass inside a container. This damper is typically installed on top of a light pole to reduce the amplitude of first-mode vibration (Desjardins et al., 2018). A chain damper can be a simple and cost-effective way to reduce buffeting-induced vibration on tall structures (Caracoglia et al., 2007). Chain dampers are made of a chain covered in rubber hanging from the top of the structure and freely moving within it, or they can be located inside a container and attached to the main structure. When the structure vibrates, the chain collides with the container's walls, resulting in alternating impulses that occur twice per cycle and dissipate the vibration's amplitude (Reed III, 1967). The effectiveness of the chain damper was tested experimentally on a full-scale 45 ft light pole and proved to increase the structure's damping (Caracoglia et al., 2007).

A tube damper typically serves to control the second mode vibration of light pole structures. This damper is made of cables with smaller strands inserted into a plastic tube. The tube damper length is usually 80% of the pole's height and can be installed through the handhole of the pole (Kaczinski et al., 1998). The tube damper was installed inside an aluminum light pole in New Jersey and increased the light pole damping from 0.18% to 0.83% (Kaczinski et al., 1998). Regarding the rod in a canister damper, it is designed to reduce higher-model vibrations typically induced by vortex shedding. It is generally installed on a height close to 2/3 of the pole, and it is ideal for retrofitting existing light poles because it can be installed inside or outside the pole (Caracoglia et al., 2007).

However, the previous vibration mitigation devices found in the literature to reduce buffeting-induced vibration are not suitable for the HMIP structures considered in this study due to several practical constraints. First, the HMIP structures are 100 ft tall, and the damper must be installed in situ. Second, the HMIP is equipped with a lowering device for installing and replacing lights at the top of the pole, so the damper installation and operation cannot interfere with the lowering device. Third, the damper must be low-cost to be economically feasible. As a result, the previously reviewed dampers, such as the ball damper, chain damper, and tube damper, will either be too difficult to be installed at the top of the pole or interfere with the lowering device. Therefore, a passive structural damper called a constrained layer damper (CLD) was chosen to reduce the HMIP vibration from buffeting as it can increase the damping of the HMIP without interfering with the lower device and is relatively easy to install at the lower portion of the HMIP. More detailed descriptions and discussions on the CLD are provided in the following sections.

A. Constrained Layer Damper (CLD)

A CLD is made of a viscoelastic (VE) material confined between the base structure and a stiff constraining layer, as illustrated in Figure 3-1 (a). When the structure vibrates in bending, the VE material deforms in shear due to relative displacement between the VE material and the base structure, as shown in Figure 3-1 (b). The shear deformation occurs in the VE material because of the separation of the neutral axes between the base structure and the constraining layer, which allows them to move differently in the longitudinal direction. As a result, the developed shear strain in the VE layer will reduce the vibration amplitude because of the VE material's ability to store shear strain energy and dissipate it via hysteresis when the beam deforms in bending.

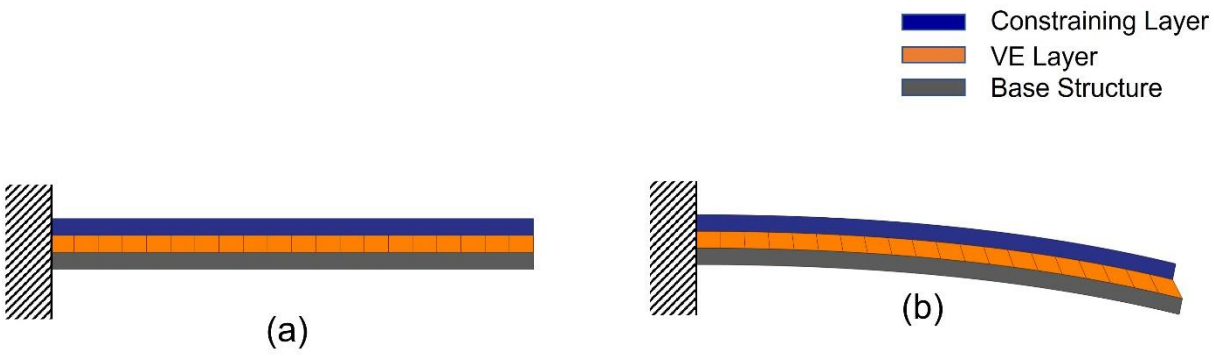

Figure 3-1 Rectangular cantilever beam (a) Undeformed VE layer; (b) Shear deformation in the VE under bending of the beam

The CLD has been widely used in mechanical and aerospace structures to efficiently reduce noise and vibrations. Previously, CLD showed effective damping when applied to rectangular cantilever beams and plates (Hujare et al., 2014; Karim, 2009; Pirk et al., 2014). However, there have been limited studies of the CLD applied to curved structures, such as tubular and cylindrical structures, and the CLD has not yet been installed on tapered, slender

tubular structures such as the HMIP. Therefore, this study will investigate the effectiveness of using a CLD in reducing vibration caused by wind-induced buffeting on HMIP structures.

3.1.2 Viscoelastic Material

The middle layer of the CLD is made of a VE material, which exhibits elastic solid and viscous liquid properties. When a material is purely elastic, all of the energy stored during the loading phase is recovered upon unloading, and the material returns to its original configuration. On the other hand, a viscous material deforms under applied load, and the stored energy does not recover after the load is removed.

The behavior of viscoelastic materials lies between the elastic and viscous extremes. Because viscoelastic materials are polymers with long chain molecules, they can convert mechanical energy into heat when deformed. Consequently, some strain energy is recovered when the load is removed, while the rest is dissipated through heat. The rate of shear energy loss in terms of thermal energy determines the viscoelastic material's performance in reducing vibration. The damping in viscoelastic materials is expressed by the phase shift between maximums of shear stress and shear strain, which has a maximum value of 90 degrees. The greater the phase angle between the stress and strain during the same cycle, the more the viscoelastic material can reduce undesired vibration (Pirk et al., 2014).

A complex modulus describes viscoelastic material behavior, a function of temperature and frequency (Hujare et al., 2014). The complex modulus describes the stiffness and damping properties of the material, and it is written as:

$$E^* = E_1 + E_2 i = E\,(1 + i\eta) \tag{3-1}$$

$$G^* = G_1 + G_2 i = G\,(1 + i\eta) \tag{3-2}$$

where E^* and G^* are the complex elastic and shear modulus. The real part of this complex modulus refers to the material's elastic behavior and defines the stiffness. The imaginary part refers to the material's viscous behavior and represents its ability to dissipate energy, which is associated with the loss factor (η).

The viscoelastic behavior can be expressed using the Maxwell and Voigt (Kelvin) models (Jones, 2001), as shown in Figure 3-2. The Maxwell model consists of a spring and a dashpot in series. When the load is applied to a Maxwell model, it causes a sudden deflection in the spring, followed by creep in the dashpot. In comparison, the Voigt model consists of a spring and a dashpot in parallel. In the Voigt model, the viscous behavior of the dashpot will not cause an immediate deflection in the spring. As a result, the deformation increases gradually, with the spring bearing most of the load while the dashpot displacement relaxes exponentially. In Abaqus CAE, the mechanical behavior of the VE material is defined using a dimensionless time-dependent shear relaxation modulus, which is dependent on the generalized Maxwell model (ABAQUS, 2021). The generalized Maxwell model, as shown in Figure 3-3, illustrates the general linear model for viscoelasticity as it is made of multiple Maxwell models connected in parallel; therefore, the shear relaxation will develop gradually over time.

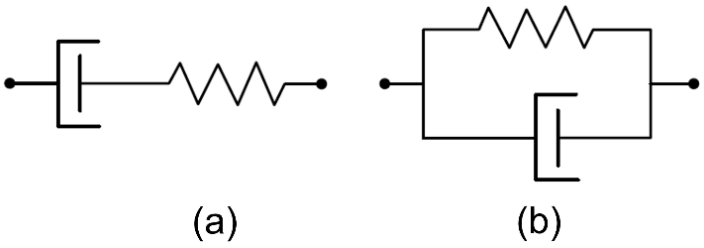

Figure 3-2 (a) Maxwell model; (b) Voigt (Kelvin) model

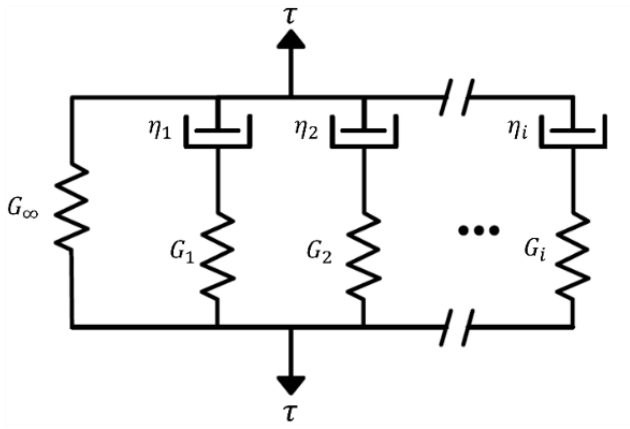

Figure 3-3 The generalized Maxwell model

3.2 Methodology

3.2.1 Overview

This section describes a numerical investigation into the efficiency of applying the CLD on tubular cantilever structures. In addition, it proposes a new method to overcome the challenges found with using the traditional CLD in this application. To this end, a new design of CLD for cylindrical sections is proposed by adding multiple longitudinal slits in the constraining layer instead of wrapping it as one piece around the circular section. This proposed method makes the CLD works effectively as a viscoelastic damper when the structure deforms in bending, which will be described in detail later in this section.

Three different models were created in Abaqus CAE, version 6.24 (ABAQUS, 2021). The efficiency of the CLD for vibration mitigation was assessed based on the damping ratio estimated from the simulated free vibration response using the logarithmic decrement method. First, a rectangular cantilever beam model was used to assess the damping capabilities of different VE materials. Then, a prismatic tubular cantilever beam model was used to compare the behavior of the conventional CLD and the proposed CLD. In the prismatic tubular cantilever beam, the effect of changing several design parameters of the CLD on its damping performance

was investigated, including the thicknesses of the VE and constraining layers and the percent coverage in the longitudinal direction. Subsequently, the proposed CLD was applied to a full-scale HMIP structure numerically. A parametric study was carried out on the effect of changing the VE layer and the constraining layer thickness to select optimal parameters for the CLD. A practical adjustment was then made to the CLD to avoid covering the area of the handhole of the HMIP, and the impact of the practical adjustment was assessed. Finally, to better understand the practical implication of the improvement in damping ratio, the study theoretically evaluated the level of reduction of the steady-state response when the HMIP is subject to resonance at the first model under buffeting-induced wind load.

3.2.2 Proposed CLD vs. Conventional CLD

The most common applications of CLD are on rectangular beams and plates (Hujare et al., 2014; Karim, 2009; Pirk et al., 2014). These studies have clearly demonstrated the CLD's ability to dampen undesired vibrations efficiently. On cylindrical sections, Li et al. (2016) experimentally tested the effect of applying different pieces of CLD on the damping ratio for high-stiffness, thin cylindrical shells. The study investigated the application of CLD to a thin cylindrical shell by varying the number of CLD pieces, the size of each CLD piece, and covering a CLD ring at various positions. The size of each CLD piece was determined by changing the length-width ratio of the CLD piece along the length or circumferential direction of the shell. The study found that the CLD increased the damping of the thin cylindrical shell, mostly when the CLD piece was applied along the circumferential direction with a length-width ratio equal to 1:6 (Li et al., 2016). Other studies used conventional CLD made of continuous constraining and viscoelastic layers wrapped around tubular structures. For instance, Karim (2009) numerically studied the application of CLD on highway bridge columns with circular sections. The study

evaluated the effect of varying the CLD coverage and the VE layer thickness on increasing the damping of the column. They found that a 0.1 in. VE layer thickness covering 40% of the column and anchored to the fixed base reduced the out-of-plane and in-plane frequency response ratios by 14% and 11%, respectively (Karim, 2009). The study also showed that the VE layer was more effective when covering 20% to 80% of the column height (Karim, 2009). Another study looked into applying CLD to reduce the vibration of a cylindrical composite structure with low vibration frequency (Kliem et al., 2019). The study looked into different scenarios of applying only the VE layer and CLD to the cylinder's inner or outer circumference and adding shear webs to the cylinder, and studied the effect of covering the shear webs with CLD. Among all the different models, the study found that the maximum damping values were achieved when the CLD was applied inside and outside the cylinder's circumference (Kliem et al., 2019). Additionally, the study found that adding a one-shear web covered with CLD along with covering the inner and outer circumference with CLD will produce the highest the obtained damping ratio (Kliem et al., 2019).

However, there is limited knowledge regarding applying CLD to slender cantilever tubular structures. In this section, the study looked into applying CLD to slender tubular cantilever structures with a low-frequency vibration.

The traditional CLD comprises a continuous constraining layer. Therefore, the base structure and the constraining layer will share the same neutral axis in tubular sections. As a result, when the structure vibrates in bending, the base structure and the constraining layer will undergo the same bending deformation, as illustrated in Figure 3-4 (a). Consequently, this results in a negligible shear deformation in the VE layer and makes the damper ineffective in dampening vibrations.

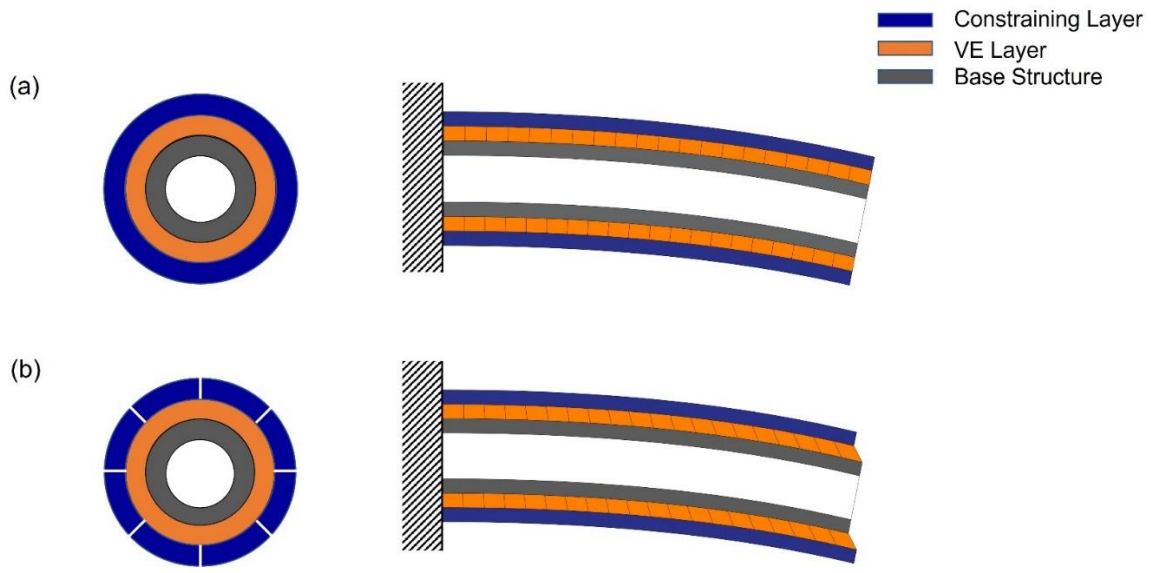

Figure 3-4 Illustration of shear deformation in the VE layer on a tubular section for (a) the conventional CLD; (b) the proposed CLD

To overcome this challenge, the proposed CLD incorporates eight longitudinal slits in the constraining layer, dividing the constraining layer into eight pieces that are continuous in the longitudinal direction of the cylinder. The advantage of this new approach is that each piece is independent of the other; therefore, the constraining layer neutral axis no longer overlaps with the base structure. As a result, this new approach allows the viscoelastic layer to develop shear deformation when the structure vibrates in bending, as shown in Figure 3-4 (b), due to the relative displacement between the constraining layer and the base structure. The proposed method allows the full engagement of the viscoelastic layer in shear, leading to higher damping. Moreover, implementing the proposed method in practice is easier than having one piece of the constraining layer covering the whole tubular structure.

The following sections include detailed analysis and results to validate the effectiveness of the proposed CLD design concept, in addition to a series of verifications to assess the damping improvement for different VE materials and the effect of changing different CLD parameters on the damping improvement in the tubular section.

3.2.3 Numerical Modeling Approach

A. Material Properties

The base structure in each finite element (FE) model was made of steel. The constraining layer was made of steel in the rectangular cantilever beam model and the prismatic tubular cantilever beam. However, in the HMIP model, the constraining layer was made of carbon fiber-reinforced polymer (CFRP). Regarding the VE material, a comparison of three VE materials will be made in the rectangular cantilever beam section to choose the material with the highest damping capability for the cylindrical sections.

The nonlinear time-dependent behavior of the VE material was simulated in Abaqus using hyperelastic and viscoelastic properties. The hyperelastic properties illustrate the rubber's instantaneous elastic modulus undergoing significant deformation. It can be defined in Abaqus by providing the strain-energy potential coefficients or by fitting data from uniaxial, biaxial, planner, and volumetric tension and compression tests (ABAQUS, 2021). The material's test data is fitted to an Abaqus-defined strain-energy potential, which includes the Arruda-Boyce, Marlow, Ogden, Polynomial, Van der Waals, Mooney-Rivlin, Reduced Polynomial, Neo-Hookean, and Yeoh models (ABAQUS, 2021).

The viscoelastic properties define the rubber's long-term viscous response. In Abaqus, the Prony series is used to model the stress relaxation response in viscoelastic materials, or it can be defined by fitting shear test data to the Prony series parameters. The shear relaxation Prony series for a generalized Maxwell model is given by:

$$G(t) = G_{\infty} + \sum_{i=1}^{N} G_i \, e^{-t/\tau_i} \tag{3-3}$$

where G_∞ is the long-term shear modulus of a material when it is completely relaxed. The shear modulus of the i[th] element is given by G_i, and the relaxation time τ_i is the ratio of viscosity (η_i) over G_i.

The initial relaxation modulus $G_0 = G_\infty + \sum_{i=1}^{N} G_i$. Therefore,

$$G(t) = G_0 - \sum_{i=1}^{N} G_i + \sum_{i=1}^{N} G_i\, e^{-\frac{t}{\tau_i}} = G_0 - \sum_{i=1}^{N} G_i \left(1 - e^{-\frac{t}{\tau_i}}\right) \tag{3-4}$$

In Abaqus, the dimensionless shear relaxation modulus, $g_R(t)$, is given as $\frac{G(t)}{G_0}$. Thus,

$$g_R(t) = 1 - \sum_{i=1}^{N} g_i \left(1 - e^{-\frac{t}{\tau_i}}\right) \tag{3-5}$$

where g_i is the dimensionless Prony series coefficient, which is equal to $\frac{G_i}{G_0}$.

B. Meshing and Tie Constraints

The base structure and the constraining layer were modeled using the eight-node linear brick element (C3D8). VE and rubberlike materials have a high Poisson's ratio close to 0.5 because they are considered almost incompressible. Therefore, a hybrid deformable C3D8H element was used for the VE layer. A hybrid element adds a degree of freedom to measure the stress considering there is no change in the volume of the material under load. The C3D8 elements are eight-node, 3D-solid elements with 24 degrees of freedom in terms of displacement. However, the C3D8 element might experience shear locking and extra stiffness caused by the Poisson's effect in bending (ABAQUS, 2021). Therefore, incompatible modes elements (C3D8I) and (C3D8IH) with an extra 13 internal degrees of freedom were modeled, and the difference in terms of free vibration response between the two mesh types is evaluated in section 3.3.

Tie constraints were used to connect the various surfaces of the beam and CLD parts. Therefore, the master surfaces were modeled as the base structure's (rectangular beam) top or

(the tubular section) outer surface and the constraining layer's bottom or inner surface. The VE material surfaces were modeled as slave surfaces, with the bottom or inner surface tied to the base structure and the top or outer surface tied to the constraining layer. In addition, the nodes were aligned in the three CLD sections, as shown in Figure 3-5.

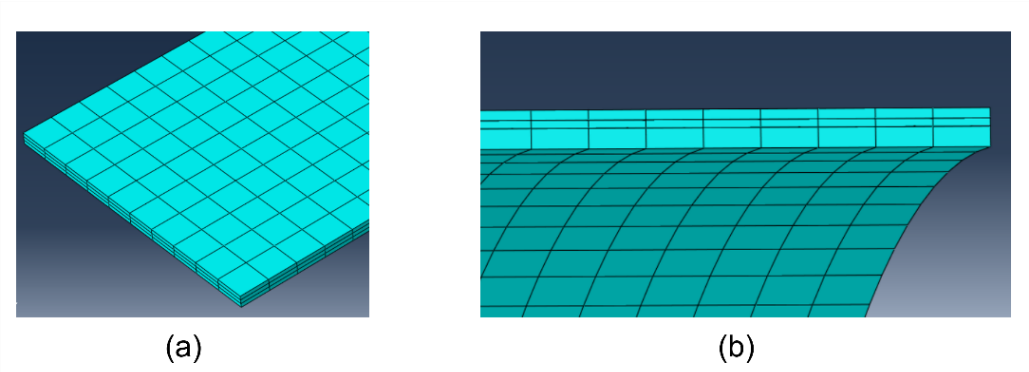

Figure 3-5 (a) Rectangular beam mesh; (b) Cross section in the cylindrical section mesh

C. Boundary Conditions and Loading

All translational and rotational degrees of freedom at the base of the cantilever beams were constrained to provide fixed boundary conditions. The constraining layer was anchored at the base using the same boundary conditions as the fixed base. Anchoring the constraining layer to the fixed support will lead to shear strain accumulation towards the free end of the VE material (Karim, 2009), thus maximizing the effectiveness of the CLD.

The load was applied as a point load at the structure's free end to cause an initial displacement equal to 1% of the structure's total height to simulate the level of wind-induced displacement captured from the videos of the HMIP. The point load was applied to the middle node of the rectangular beam. Similarly, the load was applied to a reference node at the top of the HMIP. The reference node was located in the middle of the circular section, and the circumferential surface was tied to the reference node using coupling constraint without constraining any of the nodes' degrees of freedom.

D. Implicit Dynamic Analysis

At first, a static step was applied to cause the initial displacement and then deactivated for the dynamic implicit step. The direct integration dynamic implicit step in Abaqus CAE was used to simulate the transient free vibration response caused by the applied initial displacement. The time increment value in the implicit step was set to be equal to or less than 10% of the typical period of vibration, which is the first mode's period. The time increment value ensured that no artificial damping was added from the solver to the simulated displacement time history (ABAQUS, 2021). The dynamic implicit step uses the Hilbert-Hughes-Taylor operator, an extension of the trapezoidal rule (ABAQUS, 2021). The integration matrix is inverted, and a set of simultaneous nonlinear dynamic equilibrium equations is solved at each time increment iteratively using Newton's method (ABAQUS, 2021).

3.3 Rectangular Cantilever Beam

A rectangular cantilever beam was used as a baseline to evaluate the efficiency of three viscoelastic materials in reducing the beam's vibration amplitude. The damping ratio was estimated using the logarithmic decrement method applied to the displacement free vibration time history. The material with the highest damping ratio was chosen for the rest of the study.

3.3.1 Geometry and Material Properties

The dimensions of the beam are 2 in. × 15.5 in. × 0.08 in. The VE material and the constraining layer, both with thicknesses of 0.04 in. and 0.08 in., covered the entire length of the rectangular beam. In the rectangular cantilever beam model, the constraining layer's thickness was set to be the same as the base structure to improve the efficiency of the CLD by maximizing the shear strain distribution in the VE material (Hujare et al., 2014). Table 3-1 shows the material properties of the steel used for the beam and the constraining layer.

The chosen VE materials for the rectangular cantilever beam model are based on previously used VE materials in CLD and available data in the literature for material input in Abaqus. The modeled three VE materials include vulcanized natural rubber, high-damping rubber (HDR), and Sorbothane viscoelastic polymer.

Table 3-1 Material properties of steel

Density (lb/in^3)	Young's modulus (ksi)	Poisson's ratio
0.284	29,000	0.3

A. Vulcanized Natural Rubber

Natural rubber is a material with a low damping coefficient. Vulcanizing natural rubber with sulfur improves the material's behavior by increasing its tensile strength and resistance to swelling and abrasion, and it becomes more elastic over a wide temperature range (Kakolvand et al., 2022). The hyperelastic behavior of the vulcanized rubber was defined using the Yeoh model strain-energy function based on nominal stress and nominal strain data from uniaxial, planar, and biaxial tests (Kakolvand et al., 2022). The Yeoh model is a third-degree polynomial strain-energy function and can be written as:

$$U = \sum_{i=1}^{3} (C_{i0}\left((\bar{I}_1 - 3)^i\right) \; + \sum_{i=1}^{3} \frac{1}{D_i} (J_{el} - 1)^{2i} \tag{3-6}$$

where the shear modulus is described in C_{i0}, and the initial bulk modulus K_0 is equal to $\frac{2}{D_1}$, D_i is equal to zero for incompressible materials. I_1 is the deviatoric strain's first invariant, and the elastic volumetric strain of the material $J_{el} = \frac{\lambda_1 \lambda_2 \lambda_3}{V_r}$. The Prony series for the shear relaxation data represents the vulcanized rubber viscoelasticity. Table 3-2 shows the hyperelastic properties

of the vulcanized natural rubber. Table 3-3 shows the vulcanized natural rubber viscoelastic properties.

Table 3-2 Yeoh hyperelastic model coefficients for vulcanized natural rubber

C_{10} (psi)	C_{20} (psi)	C_{30} (psi)	D_1 (psi^{-1})	D_2 (psi^{-1})	D_3 (psi^{-1})
46.412	0.00643	0.01878	1.5057×10^{-5}	5.9856×10^{-7}	-1.2369×10^{-7}

Note: the vulcanized natural rubber hyperelastic coefficients are adopted from Kakolvand et al. (2022).

Table 3-3 Prony series parameter for vulcanized natural rubber

g_1	g_2	τ_1	τ_2
0.094	0.094	0.09	0.045

Note: the vulcanized natural rubber Prony series parameters are adopted from Kakolvand et al. (2022).

B. High-Damping Rubber (HDR)

Rubber has been widely used in the seismic protection of structures throughout VE dampers and base isolation systems. The need to increase the damping in natural rubber led to HDR production by adding fine carbon black, oils or polymers, and other additives to the natural rubber (Ibrahim et al., 2007). The Ogden model strain-energy function was used to define the HDR hyperelastic material behavior base on uniaxial test data (Modhej et al., 2021), which can be written in this form:

$$U = \sum_{i=1}^{3} \frac{2\mu_i}{\alpha_i^2}\left(\bar{\lambda}_1^{\alpha_i} + \bar{\lambda}_2^{\alpha_i} + \bar{\lambda}_3^{\alpha_i} - 3\right) + \sum_{i=1}^{3} \frac{1}{D_i}(J_{el} - 1)^{2i} \tag{3-7}$$

where α_i is the dimensionless non-linearity constant, the initial shear modulus (μ) given by $\sum_{i=1}^{3} \mu_i$, and the initial bulk modulus K_0 equal to $\frac{2}{D_1}$, D_i is equal to zero for incompressible materials. The deviatoric stretches $\bar{\lambda}_i = J^{-\frac{1}{3}}\lambda_i$, in which λ_i are the principal stretches, and the elastic volumetric strain of the material $J_{el} = \frac{\lambda_1\lambda_2\lambda_3}{V_r}$. The viscoelastic behavior was defined using

the Prony series parameters, which are time-dependent constants based on a shear relaxation test. The viscoelastic and hyperelastic properties of HDR are provided in Table 3-4 and Table 3-5, respectively.

Table 3-4 Prony series parameter for HDR

$g_i \times 10^{-2}$	τ_i
9.88	0.01
-5.36	0.10
25.19	1
4.02	10
16.53	100

Note: the HDR Prony series parameters are adopted from Modhej et al. (2021)

Table 3-5 Uniaxial test data for HDR

Stress (psi)	Strain (%)
-411.473	-42
-242.794	-30
-140.832	-20
-91.519	-15
-38.5801	-10
0	0
353.8927	100
706.3351	200
1138.548	300
1699.845	400
2313.356	500

Note: the HDR uniaxial test data are adopted from Modhej et al. (2021)

C. Polyurethane Viscoelastic Material

The Sorbothane VE polymer used in this section is made of polyurethane material. This material has unique properties such as long fatigue life, low creep coefficient, shock absorption for millions of cycles, and high damping coefficient over a wide temperature range of -20 F to 160 F (Sorbothane Inc., 2022). The Sorbothane weight density is 0.048 lb/in^3. The VE polymer's instantaneous elastic modulus is calculated using hyperelastic properties and the Ogden model strain-energy function described in Equation (3-7). The hyperelasticity is defined in Abaqus CAE using uniaxial test data, which is provided in Table 3-6. Furthermore, the viscoelastic

properties using the Prony series represent the long-term viscous response, which can be found in Table 3-7.

Table 3-6 Uniaxial test data for Sorbothane VE material

Stress (psi)	Strain
7	0.1
11	0.15
19	0.2
24	0.25
48	0.3
69	0.4

Note: the Sorbothane VE material uniaxial test data are adopted from Al-Rumaih (2009)

Table 3-7 Prony series parameter for Sorbothane VE material

g_1	g_2	τ_1	τ_2
0.6281	0.1908	0.0202	0.1819

Note: the Prony series parameters are adopted from Al-Rumaih (2009)

3.3.2 Material and Element Type Evaluation

A. VE Materials Damping Ratio

The VE material evaluation was based on the displacement's free vibration response obtained from the implicit step in Abaqus. The logarithmic decrement method was used to get the damping ratios of the three VE materials. Figure 3-6 shows that the vulcanized natural rubber had the lowest damping ratio, estimated to be 0.72%. The HDR material performed better than the vulcanized natural rubber in reducing the vibration amplitude, and its damping ratio was estimated to be around 1.06%. Regarding the Sorbothane VE material, the material was able to damp out the vibrations quicker than the vulcanized natural rubber and the HDR. The damping ratio of the Sorbothane VE material was around 2.95%. Table 3-8 summarizes the damping ratios obtained from the three VE materials. Because Sorbothane had the highest damping performance among the vulcanized natural rubber and HDR, it was chosen as the VE material for this project.

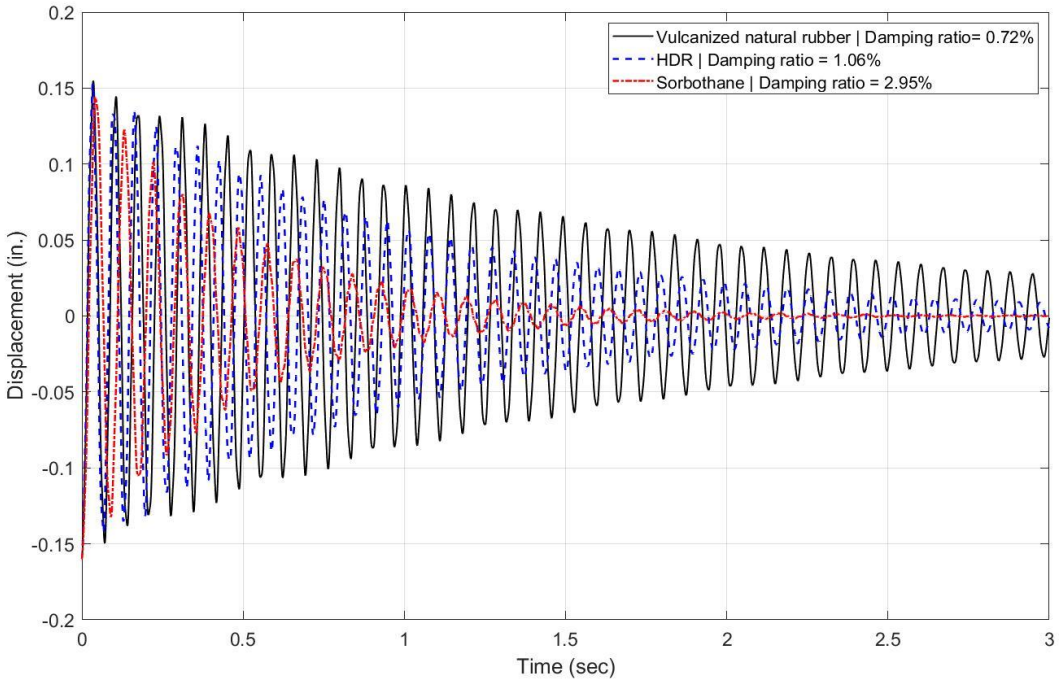

Figure 3-6 Free vibration displacement response for the rectangular cantilever beam with three different VE materials

Table 3-8 Damping ratio for the three different VE materials

Material	Damping ratio (%)
Vulcanizing natural rubber	0.72
High-damping rubber	1.06
Sorbothane	2.95

B. Evaluation of Element Type

The Poisson's effect in bending may cause shear locking and extra stiffness in the eight-node linear brick element. This research focused on estimating the damping response from the free vibration response of the CLD. Therefore, this section evaluates the free-vibration response from the eight-node brick element (C3D8) mesh type and the eight-node brick element with incompatible modes (C3D8I) mesh type.

The C3D8I mesh type is simulated for the rectangular cantilever beam model with the Sorbothane material using a dynamic implicit step, followed by a damping ratio evaluation using

the logarithmic decrement method. Figure 3-7 shows that the C3D8 mesh produced a damping ratio of 2.97%, whereas the C3D8I mesh produced a damping ratio of 3.12%. Considering the minimal difference in damping ratio between the two mesh types and the additional time required to run the incompatible modes elements, the C3D8 element is chosen. Moreover, the C3D8 element also provides a more conservative damping estimation compared to the C3D8I element.

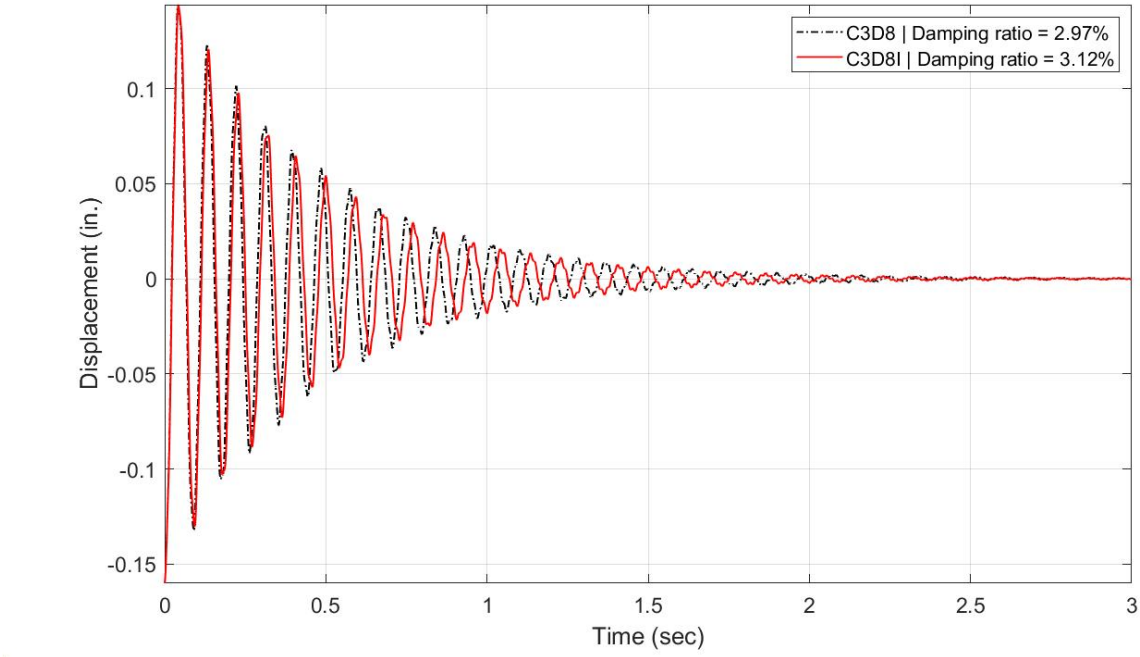

Figure 3-7 Mesh evaluation for the C3D8 and C3D8I elements

3.4 Tubular Cantilever Beam

This section discusses the conventional and proposed CLD on a prismatic tubular cantilever beam and provides numerical simulations to show the effectiveness of adding multiple longitudinal slits to the constraining layer. A parametric study was conducted to see the effect of changing a few parameters on reducing the free vibration response of the prismatic tubular cantilever beam. To this end, the study investigates adjusting the VE material's thickness to understand better the effect of changing the VE layer thickness on the damping ratio. In addition,

the effect of changing the CLD coverage on vibration reduction was investigated for practical reasons because it is not practical to cover the entire structure in the HMIP model using the CLD.

3.4.1 Geometry and Material Properties

The hollow cantilever tube is 195 in. long, has a 3 in. inner diameter with a thickness of 0.16 in., and is made of galvanized steel. The constraining layer is made of a steel sheet with a thickness of 0.0625 in. For the VE layer thickness, (2012) recommended a 0.1 in. minimum thickness for practical applications of CLD. Therefore, an initial 0.1 in. VE layer made of Sorbothane was used, and the effects of increasing the VE material thickness and varying the length of the CLD are studied later in this section. The material properties of steel can be found in Table 3-1. The hyperelastic and viscoelastic properties of Sorbothane are provided in Table 3-6 and Table 3-7, respectively.

3.4.2 Shear Strain Distribution in the Conventional and Proposed CLDs

The conventional CLD was implemented in Abaqus CAE by wrapping a continuous constraining layer around the tubular structure, as illustrated in Figure 3-8 (a). As shown in Figure 3-9, the transient free vibration response from the implicit step showed virtually no damping. To understand the mechanical reason for this phenomenon, the shear strain distribution along the VE material was investigated using a Visco step. The Abaqus CAE Visco step is a quasi-static stress analysis used to analyze the response of time-dependent materials such as VE materials (ABAQUS, 2021). As explained in section 3.2.2, due to the overlapping of neutral axes for the base structure and the constraining layer in the conventional CLD, both the base structure and the constraining layer undergo the same bending deformation, resulting in negligible shear strain along the VE material, as shown in Figure 3-10. For this reason, the conventional CLD adds negligible damping when applied to tubular structures.

A new CLD design is then introduced to overcome this challenge by adding eight 0.04 in. wide slits to the constraining layer in the longitudinal direction, as in Figure 3-8 (b). This newly proposed CLD design splits the constraining layer into eight different pieces. Each piece of the constraining layer will act independently from others; hence they no longer share the same neutral axis with the base structure. Consequently, the VE material will fully engage and deform in shear when the cylindrical section undergoes bending deformation. In particular, the VE material's shear strain accumulates towards the free end, as shown in Figure 3-10. The newly proposed CLD effectively reduces the vibration amplitude on the tubular beam, as seen in Figure 3-9. The estimated damping ratio from the free vibration response is 2.94%.

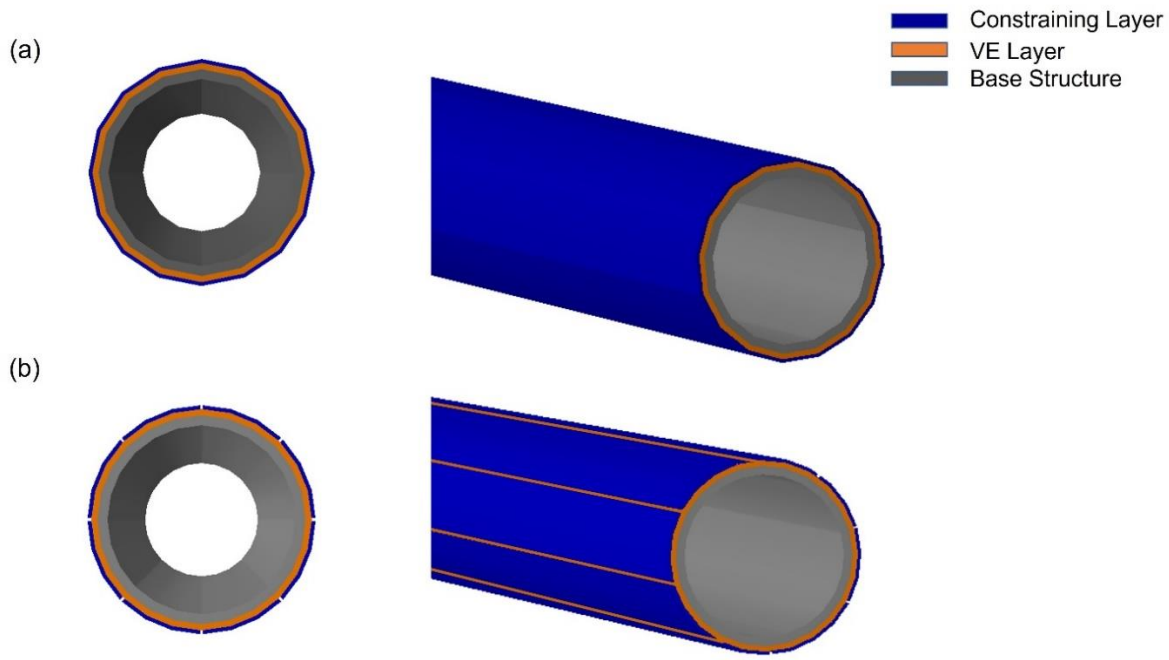

Figure 3-8 Illustration of (a) conventional CLD; (b) newly proposed CLD with slits in the constraining layer

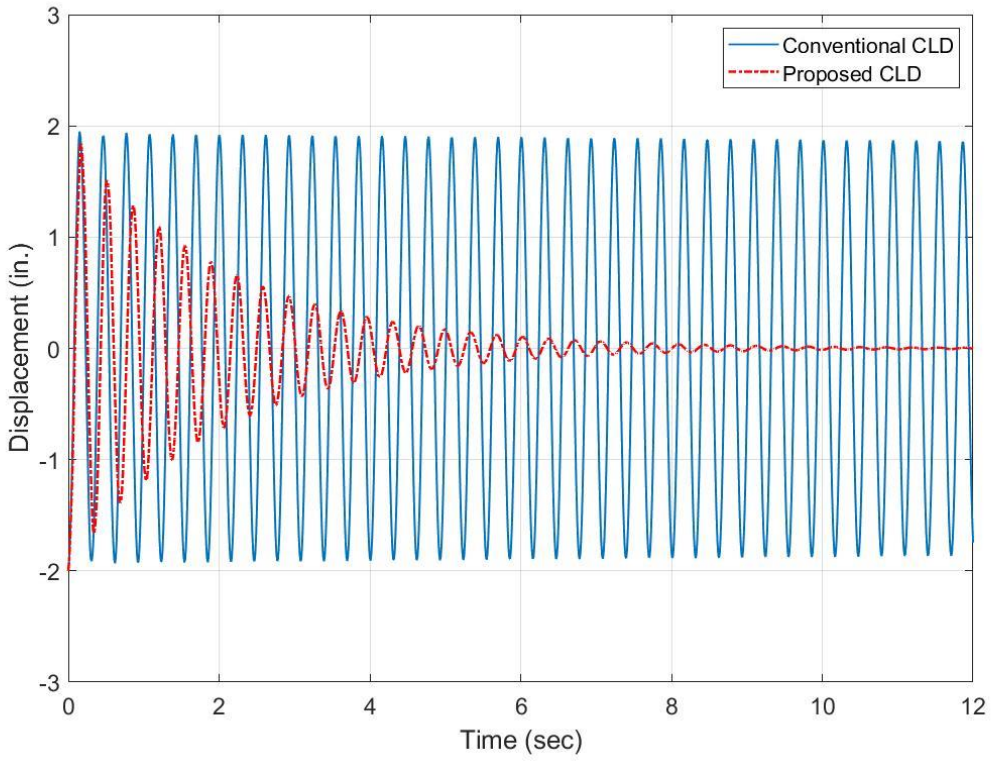

Figure 3-9 Free vibration displacement response for the conventional CLD vs. the newly proposed CLD

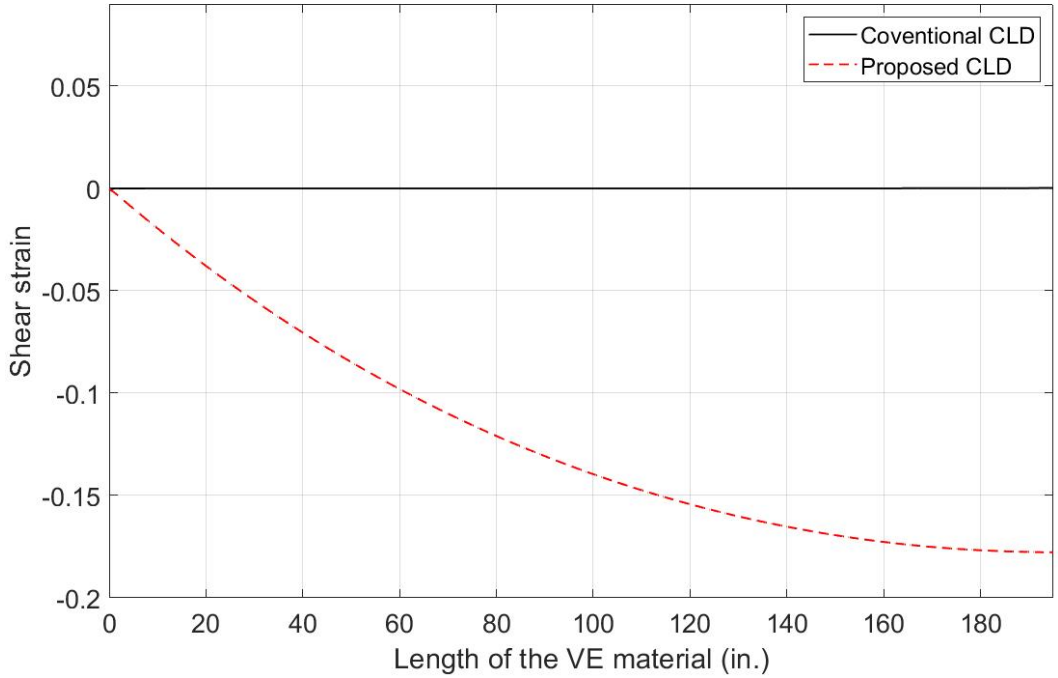

Figure 3-10 Shear strain distribution in the conventional CLD vs. the proposed CL

In addition to adding slits to the constraining layer, the study also investigated the effect of adding slits to the VE layer to divide the VE layer into separate sheets. It was discovered that the discontinuity in the VE layer had no significant effect on the damping ratio, which is illustrated in the free displacement vibration responses shown in Figure 3-11. In contrast, the constraining layer needs to be continuous in the longitudinal direction of the cylinder to force the VE material to deform in shear. Since in practice the VE material does not easily cover the whole circumference of the HMIP structure, the Abaqus models for the tubular cantilever beam and the HMIP were created by separating the VE layer, as shown in Figure 3-12.

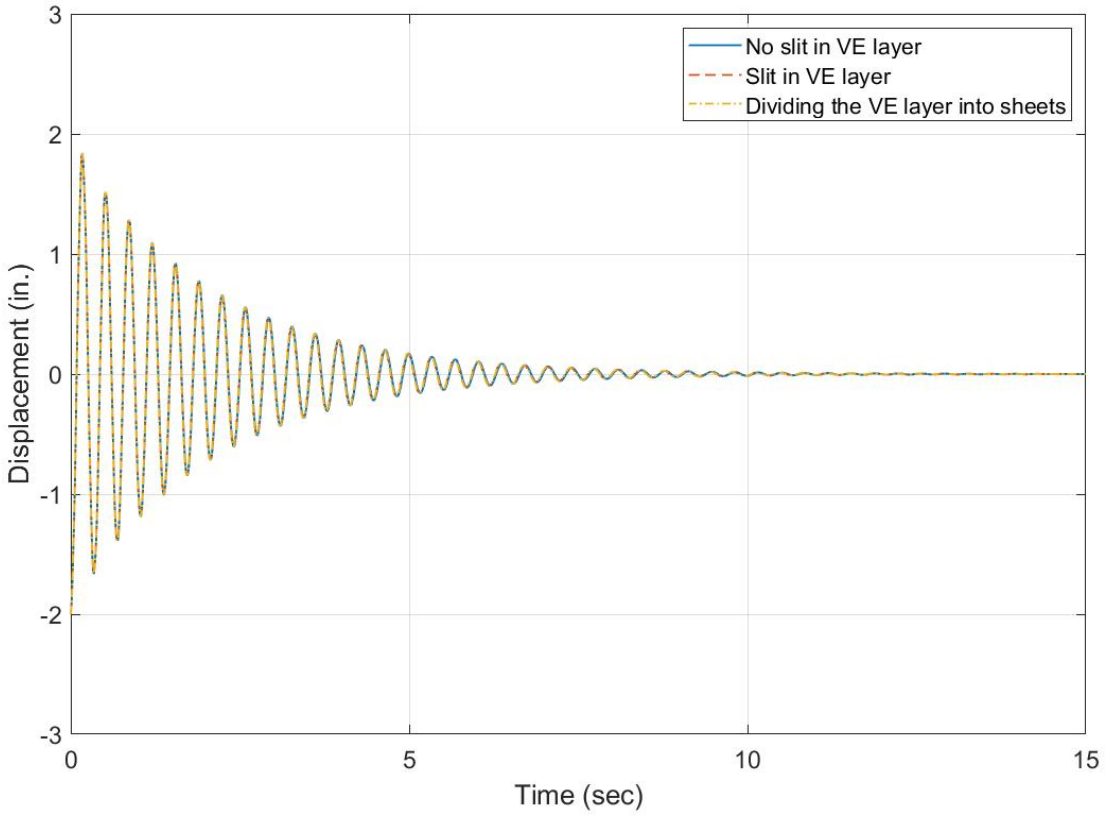

Figure 3-11 Comparison of free vibration displacement responses with and without longitudinal slits in the VE layer for the CLD

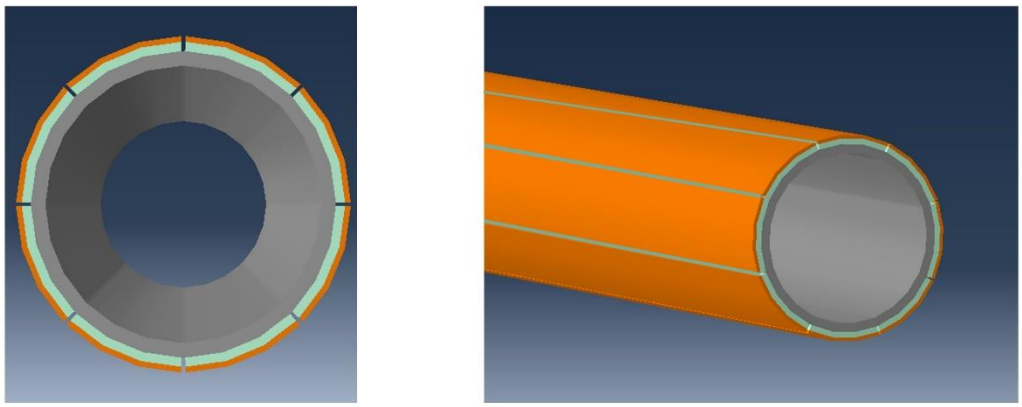

Figure 3-12 The proposed CLD with slits in both the VE and constraining layers

3.4.3 The Effect of Varying the VE Material Thickness and CLD Coverage

This section investigates the impact on the performance of the proposed CLD in reducing the vibration response by varying the VE layer thickness and changing the CLD coverage along the prismatic cylindrical cantilever beam.

Four different VE layer thicknesses (t_v) were chosen based on the manufacturer's datasheet, including 0.1 in., 0.188 in., 0.25 in., and 0.375 in. The four thicknesses were evaluated based on the free vibration response from the implicit step. From the simulation results shown in Figure 3-13, as the VE layer thickness decreases, the CLD adds higher damping to the structure, which is consistent with what Karim et al. (2012) found. According to the FE analysis, the estimated damping ratios were 2.94%, 2.66%, 2.51%, and 2.27%, respectively, associated with the selected VE layer thicknesses starting with the thinnest layer. The results are also summarized in Table 3-9.

To investigate the impact of the longitudinal coverage of the CLD, the 0.1 in. VE layer thickness was implemented for the CLD, covering 100%, 50%, and 25% of the total height of the

tubular beam, as illustrated in Figure 3-14. Figure 3-15 shows that the more coverage the CLD has, the better the damper's performance in increasing damping. Specifically, the damping ratio for 100% coverage was 2.94%, 50% coverage was 1.71%, and 25% coverage was 0.41%. Table 3-10 summarizes the achieved damping ratios based on changing the CLD coverage.

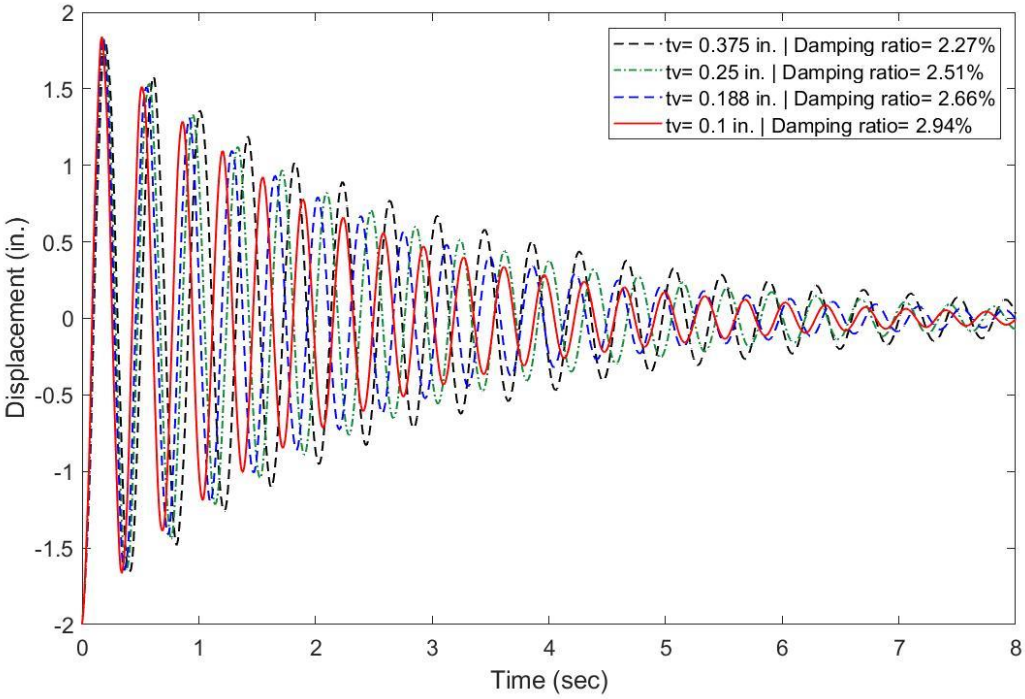

Figure 3-13 Free vibration responses for different VE layer thicknesses (t_v)

Table 3-9 Effect of changing the VE material thickness on the tubular beam's damping ratio

VE material thickness (in.)	Damping ratio (%)
0.1	2.94
0.188	2.66
0.25	2.51
0.375	2.27

Table 3-10 Effect of changing the CLD coverage on the tubular beam's damping ratio

CLD coverage (%)	Damping ratio (%)
100	2.94
50	1.71
25	0.41

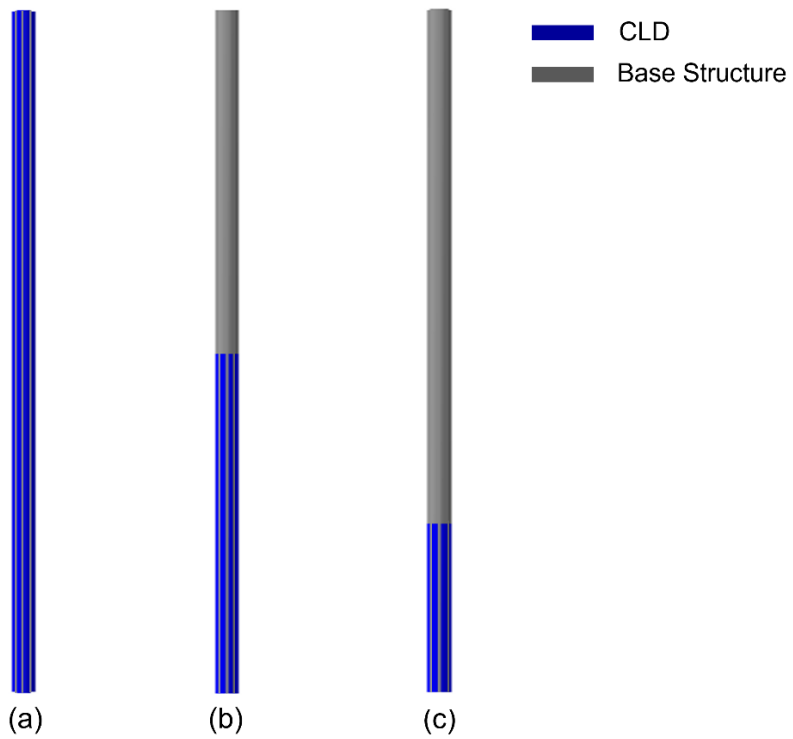

Figure 3-14 Illustration of the longitudinal CLD coverage (a) 100%; (b) 50%; (c) 25%

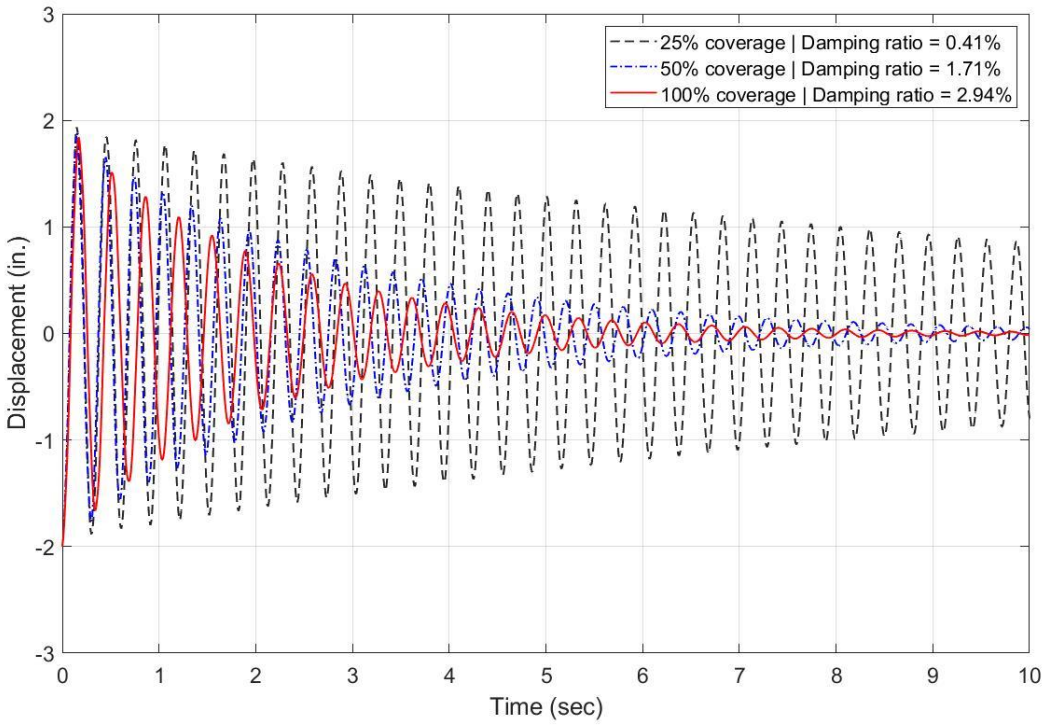

Figure 3-15 Free vibration responses for CLD with 0.1 in. VE layer covering different heights of the beam

3.4.4 Summary

A tubular cantilever beam model was used to investigate the behavior of the CLD on a circular hollow section. This model validated the effectiveness of the proposed new CLD design, which includes slits in the longitudinal direction of the constraining layer. Introducing the longitudinal slits to the constraining layer allowed an effective development of shear deformation in the VE layer and hence enhanced the damping performance of the system. In addition, results demonstrated that within the considered VE layer thicknesses, thinner VE layers achieved higher damping ratios for the CLD. In addition, the higher percentage of longitudinal coverage of the CLD introduced higher damping to the system. With the above observations, the following section will continue to assess the effectiveness of the proposed CLD on the full-scale tapered HMIP structure.

3.5 HMIP Model

The primary objective of this chapter is to develop a device that reduces wind-induced vibration on the monitored HMIP. Therefore, the proposed CLD is modeled using Abaqus CAE to cover the bottom 30 ft of the HMIP. The 30-ft coverage of the CLD is determined by a practical height the boom lift can reach, which may be used in installing the CLD in the field. This section investigates the effect of varying the VE and constraining layer thicknesses on increasing the damping to reduce the vibration amplitude of the HMIP. The study further assesses a practical adjustment to start the CLD above the HMIP handhole to avoid interference with the handhole.

3.5.1 Geometry and Material Properties

The HMIP is 100 ft tall and is made of galvanized steel with a 0.33-degree tapered hollow circular section. The light assembly weighs 406 lb at the top of the pole, which consists

of three LED fixtures and a lowering device. In the FE model, the HMIP is represented as a single section with a constant thickness of 0.25 in. and a base inner diameter equal to 25 in. Regarding the VE material, the Sorbothane VE polymer is adopted based on the study in Section 3.3, and it is modeled with different thicknesses covering the bottom 30 ft of the pole. Furthermore, the effect of changing the VE layer thickness on the damping ratio is described later in this section. A type of isotropic CFRP was chosen for the constraining layer due to its unique properties compared to steel sheets, such as lightweight, high stiffness, and ease of handling, cutting, and installation. The material properties of the CFRP are included in Table 3-11. The effect of changing the thickness of CFRP on the damping ratio is also assessed later in this section. The material properties of steel are listed in Table 3-1, while the hyperelastic and viscoelastic properties of the Sorbothane VE material are given in Table 3-6 and Table 3-7, respectively.

Table 3-11 CFRP material properties

Density (lb/in^3)	Young's modulus (ksi)	Poisson's ratio
0.067	33,495	0.1

Note: the CFRP properties are adopted from Al-Salih (2022)

3.5.2 Effect of Varying the VE Material Thickness

This section investigates how changing the VE layer thickness affects the damping ratio of the HMIP while keeping the CFRP thickness constant and equal to 0.0625 in. The Sorbothane VE polymer was modeled with four thicknesses: 0.1 in., 0.188 in., 0.25 in., and 0.375 in. The free vibration displacement response is used to estimate the damping ratio obtained for the four VE layer thicknesses.

Figure 3-16 illustrates how damping performance changes when the VE layer thickness changes. It can be seen that the highest damping ratio was achieved when the VE layer thickness

was at 0.188 in., which resulted in 0.88% damping. Increasing or decreasing the VE layer thickness will decrease the damping ratio, which correlates with a study by Karim et al. (2012). This may be explained by the fact that decreasing the VE layer thickness leads to higher shear strain in the VE layer, leading to higher energy dissipation. However, if the VE material is too thin, there is not enough VE material to dissipate the vibration energy through shear deformation. Therefore, it is important to consider this competition between the amount of VE material and the level of developed shear strain in selecting the VE layer thickness.

The HMIP's damping ratio obtained from changing the VE material thickness is summarized in Table 3-12. The damping ratio increases from 0.85% for a VE layer thickness of 0.1 in. to 0.88% when the VE thickness increases to 0.188 in. Then the damping ratio decreases to 0.79% and 0.78% for VE thickness of 0.25 in. and 0.375 in., respectively.

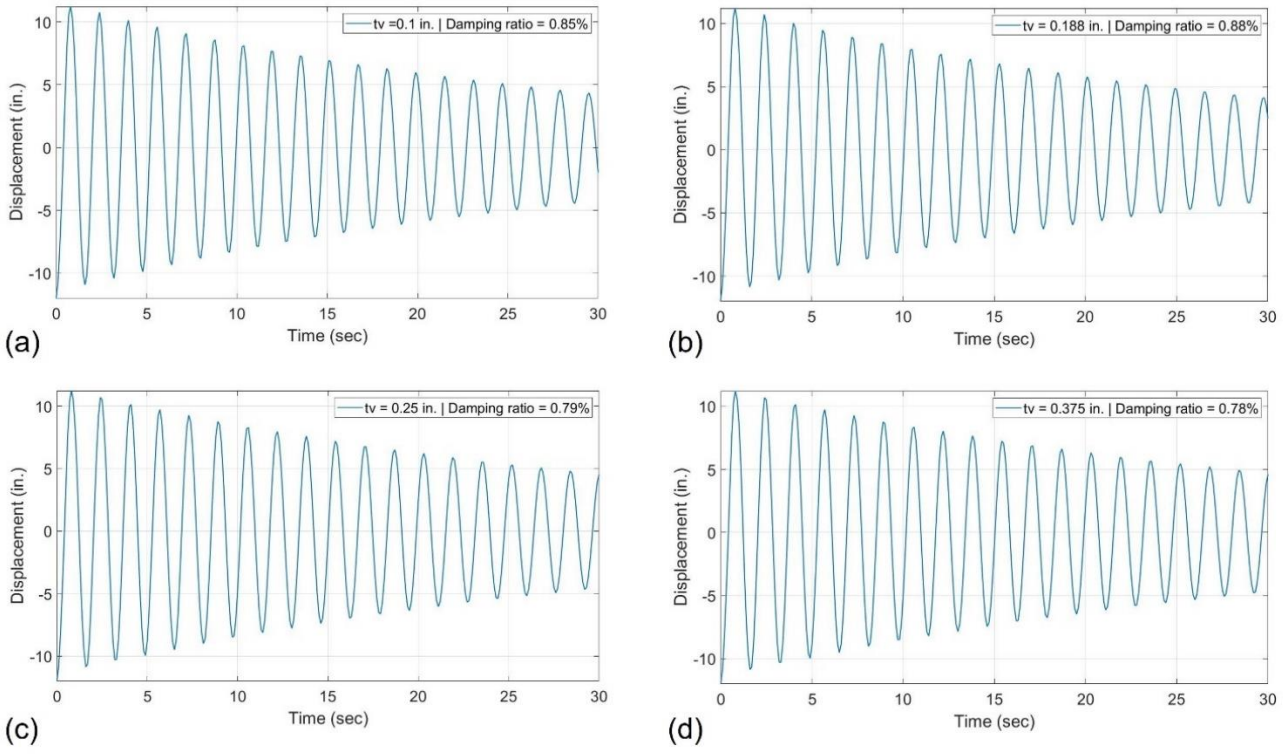

Figure 3-16 Free vibration displacement response for the HMIP model with constraining layer thickness of 1/6 in. and different VE layer thicknesses including (a) 0.1 in.; (b) 0.188 in.; (c) 0.25 in.; (d) 0.375 in.

Table 3-12 Effect of varying the VE material thickness on the HMIP's damping ratio

VE material thickness (in.)	Damping ratio (%)
0.1	0.85
0.188	0.88
0.25	0.79
0.375	0.78

3.5.3 Effect of Varying the CFRP Layer Thickness

The effect of varying the CFRP thickness on vibration reduction performance is examined while maintaining the VE layer thickness at 0.1 in. The VE layer thickness was chosen to be 0.1 in. because of its excellent damping performance without using too much VE material. The CFRP was modeled with four different thicknesses: 0.0625 in., 0.08 in., 0.1 in., and 0.125in. The reduction of the displacement amplitude was assessed to determine the damping ratio to evaluate the impact of the CFRP thickness.

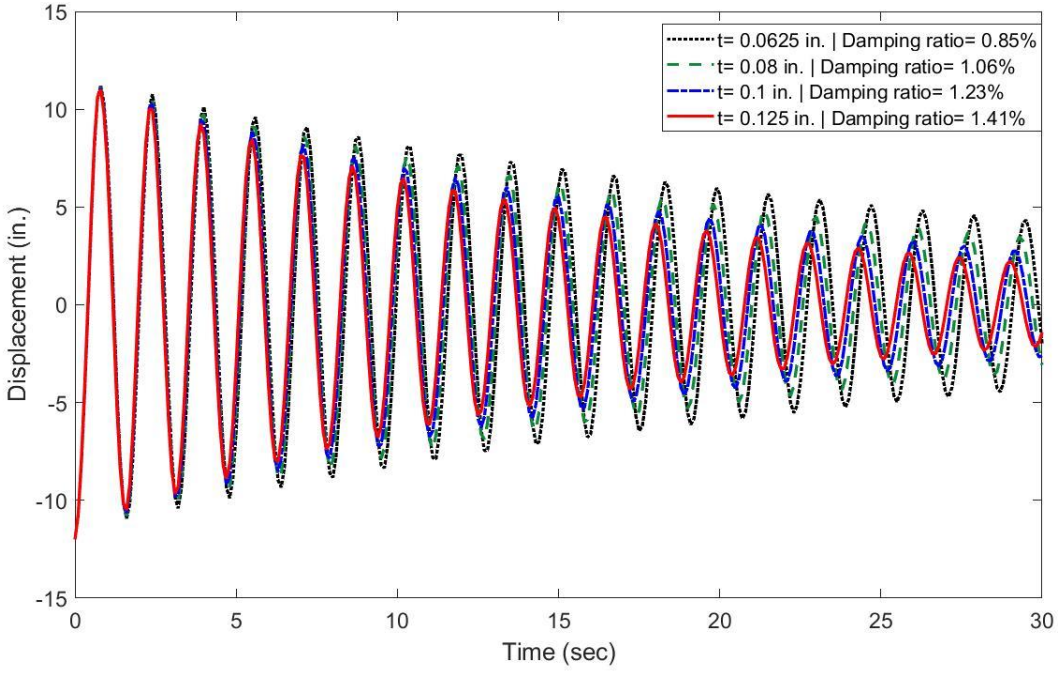

Figure 3-17 Free vibration displacement response for the HMIP model with varying CFRP thicknesses while fixing the VE layer thickness to 0.1 in.

It was noted from the free vibration response shown in Figure 3-17 that increasing the thickness of the CFRP leads to better damping performance with the CLD. The maximum obtained damping ratio is 1.41% for the CFRP thickness of 0.125 in., and the damping ratios are 1.23%, 1.06%, and 0.85% for CFRP thicknesses of 0.1 in., 0.08 in., and 0.0625 in., respectively. Table 3-13 summarizes the HMIP damping ratios corresponding to different CFRP thicknesses.

Table 3-13 Effect of varying the CFRP thickness on the HMIP's damping ratio

CFRP thickness (in.)	Damping ratio (%)
0.0625	0.85
0.08	1.06
0.1	1.23
0.125	1.41

3.5.4 Effect of a Practical Adjustment to the CLD

This section studies the effect of adjusting the CLD to start above the HMIP's handhole to avoid interference between the CLD and the handhole. Therefore, the CLD started 5 ft above the ground to avoid covering the handhole, and its total length became 25 ft instead of 30 ft, as shown in Figure 3-18. Meanwhile, the VE layer thickness is selected as 0.1 in., and the constraining layer is 0.125 in. thick, anchored at the bottom of the HMIP structure. In the FE model, the constraining layer was anchored to the HMIP using a thin CFRP sheet with a thickness of 0.0625 in. and a length of 0.225 in. covering the area beneath the constraining and VE material. As illustrated in Figure 3-19, the anchorage was made by tying the HMIP's wall to the CFRP sheet wall and tying the bottom of the constraining layer to the top surface of the sheet. This arrangement was made to simulate anchoring the constraining layer to the HMIP only for the FE model. Further investigation must be made into anchoring the constraining layer to the HMIP in practice.

Figure 3-20 compares the free vibration responses between the HMIPs with CLD starting from the base plate and one starting above the handhole. The figure demonstrates that adjusting the CLD to avoid covering the handhole reduced the damping ratio compared to when the constraining layer was anchored to the base of the HMIP. The reduction in the damping ratio is due to the loss of some CLD coverage. However, the damping ratio reduces from 1.41% to 1.08%, which is not a huge reduction. Moreover, the damping ratio introduced by the adjusted CLD is still higher than the HMIP's inherent damping, which is 0.8% as determined by the pluck test in Chapter 2. As a result, after retrofitting the HMIP, the adjusted CLD will increase the structure's total damping ratio to 1.88%, which is 235% of the inherent structural damping.

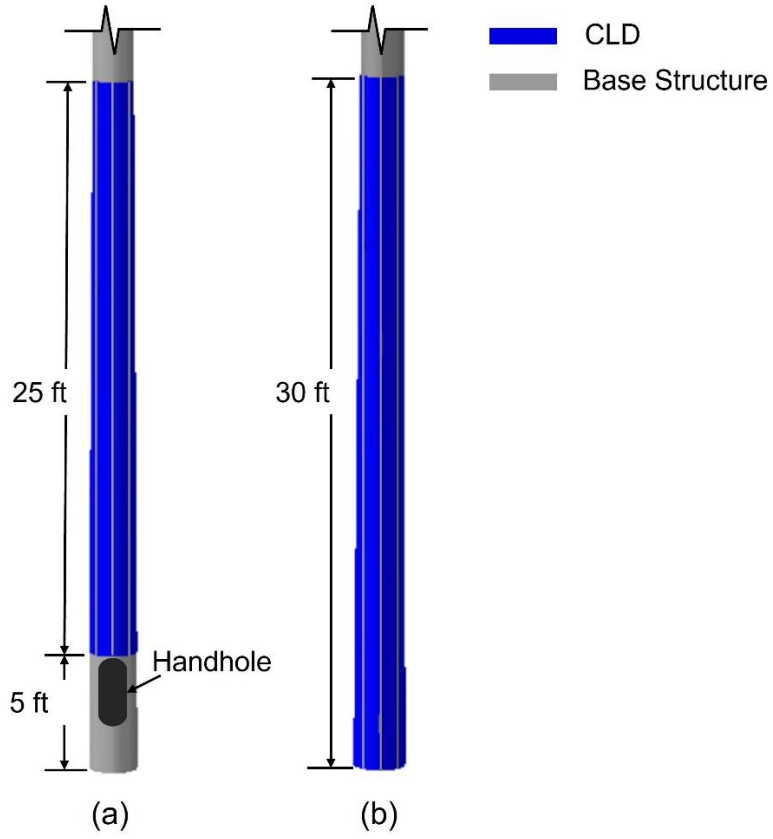

Figure 3-18 Illustration for the CLD applied to the HMIP in FE model (a) CLD not covering the handhole; (b) CLD covering the handhole

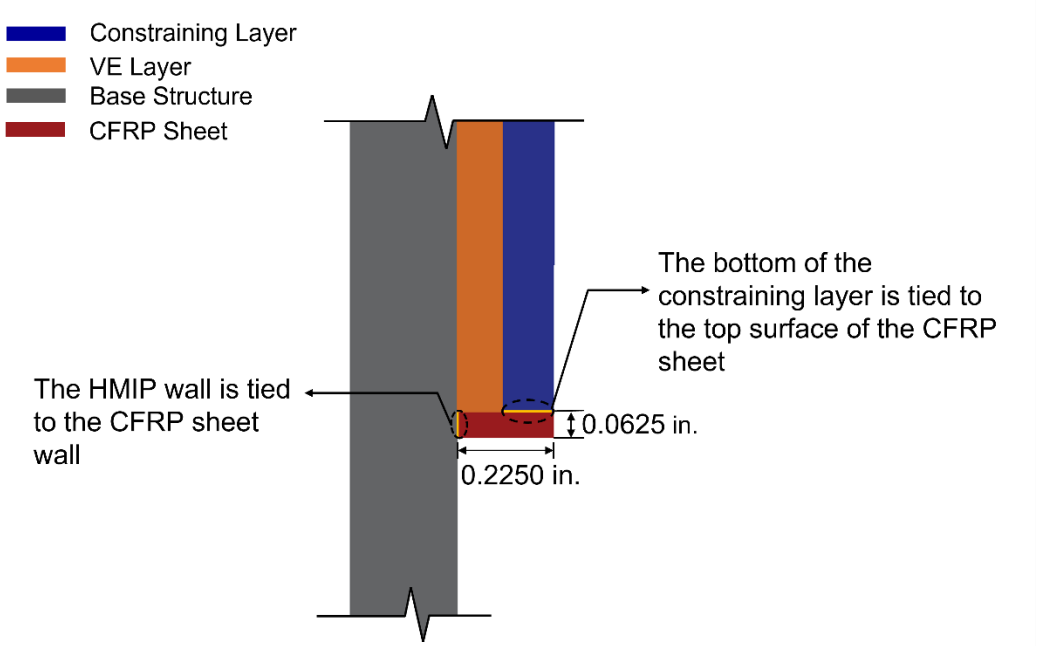

Figure 3-19 Illustration of the detail in the FE model for anchoring the constraining layer to the HMIP

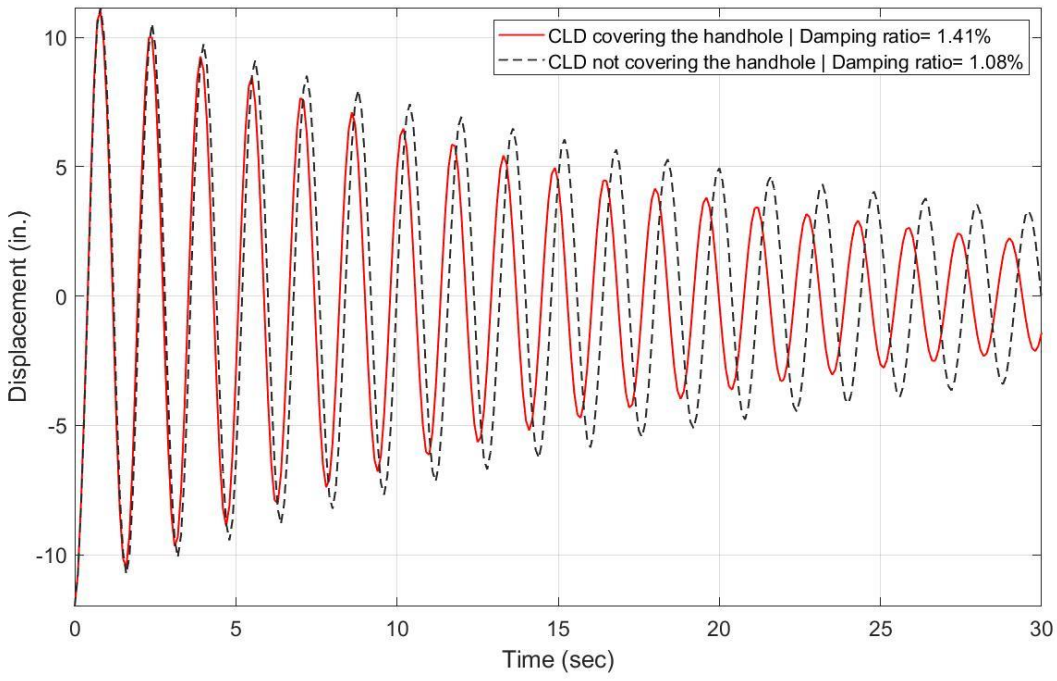

Figure 3-20 Free vibration displacement response for the proposed CLD and the adjusted CLD

3.5.5 Steady-State Response for the HMIP at Resonance

Since in this study, the wind loading becomes a concern when it triggers resonance at the first mode due to buffeting, this section evaluates the steady-state response of the HMIP under the first mode resonance under three scenarios, including 1) no CLD is used, 2) the adjusted CLD which starts above the handhole is implemented, and 3) the CLD that starts from the base plate and covers the HMIP handhole. This assessment provides a better understanding of how the previously achieved damping ratios would reduce the steady-state vibration response under the first-mode resonance produced by wind-induced buffeting.

The steady-state response reflects the amplitude and phase angle of the harmonic vibration of a single-degree-of-freedom (SDOF) system as a result of a harmonic load excitation, and it is given as $u_p = U\cos(\Omega t - \alpha)$, where U is the vibration amplitude, Ω is the excitation frequency, and α is the phase angle. Based on structural dynamics, the dimensionless amplitude of the steady-state response $\bar{H}(r)$ is given by

$$\bar{H}(r) = \frac{U}{U_0} = \frac{1}{\sqrt{(1-r^2)^2 + (2\zeta r)^2}} \tag{3-8}$$

where U_0 is the static displacement and is defined as the displacement the mass would experience if the force were applied statically. *r* is the ratio of the excitation frequency (Ω) over the natural frequency (ω_n), and at resonance *r* is equal to 1. Hence, the dimensionless amplitude of the steady-state response at resonance is given by

$$\bar{H}(r) = \frac{1}{2\zeta} \tag{3-9}$$

The inherent damping of the HMIP structure was determined to be 0.8%, while installing the adjusted CLD, which starts above the handhole, resulted in an overall damping ratio of around 1.88%. When the CLD was extended to the HMIP's base, the estimated overall damping

ratio was 2.22%. Since the amplitude of the vibration at resonance is inversely proportional to the damping ratio, as shown in Equation (3-9), the adjusted CLD would reduce the vibration amplitude by 57.4%, while the CLD that covers the handhole would reduce the vibration amplitude by 64% compared with the vibration response of the bare HMIP structure. Table 3-14 summarizes the dimensionless amplitudes of the steady-state responses at the first mode resonance of the HMIP.

Table 3-14 The dimensionless amplitude of the steady-state response at the HMIP's first mode resonance for the three CLD scenarios

Scenario	$\bar{H}(r=1)$	Reduction from no CLD case
No CLD	62.5	0%
CLD is not covering the handhole	26.6	57.4%
CLD is covering the handhole	22.5	64%

3.5.6 Summary

The proposed CLD design was tested on the HMIP structure to reduce the wind-induced vibration due to buffeting. The CLD coverage was set to 30 ft, and the free vibration was assessed by varying the thickness of the VE and CFRP layers. It was found that the optimal thickness for the VE material was 0.188 in. The damping ratio increased until the VE layer thickness reached 0.188 in. and then started to decrease as the thickness increased. Regarding the CFRP thickness, the damping ratio was positively correlated with the thickness of CFRP. In addition, adjusting the CLD to avoid the handhole reduced the damping ratio compared to the case when the CLD started from the base of the HMIP. Nonetheless, even when the CLD started above the handhole, it increased the total damping of the HMIP to 235% of its inherent structural damping. Furthermore, this section looked into the dimensionless steady-state amplitude at the HMIP's first mode resonance for three different cases, including no CLD, adjusted CLD that avoids the handhole, and the CLD that starts from the HMIP's base. It was found that the

adjusted CLD would reduce the steady-state amplitude at first mode resonance by 57.4% compared with the bare structure, while the CLD that covers the handhole would reduce the steady-state amplitude by 64%.

3.6 Conclusions

This chapter numerically investigated the use of CLD to reduce the vibration due to wind-induced buffeting on HMIPs in Kansas. First, the study assessed the conventional CLD on tubular structures and found that the traditional method of adding one continuous constraining layer around the cylindrical structure is ineffective in reducing the vibration due to the overlapping neutral axes between the base structure and the constraining layer. As a result, the study proposed a new CLD design by adding multiple slits to the constraining layer to divide it into pieces and separate the neutral axis of the base structure from those of the constraining layer pieces. The proposed CLD design allows each piece of the constraining layer to move independently from others when the base structure undergoes bending deformation. Hence, the proposed CLD allows the VE layer to fully engage in shear deformation to dissipate energy for vibration mitigation.

The chapter then investigated the selection of VE material by assessing the damping ratio from CLDs that adopt three different VE materials based on the rectangular cantilever beam model. It was found that Sorbothane VE polymer achieved a higher damping ratio compared with the HDR and the vulcanized natural rubber. Therefore, the Sorbothane VE material was used for the rest of the numerical investigations.

Subsequently, this chapter compared the conventional and the proposed CLDs in terms of the shear strain distribution along the VE layer based on the prismatic tubular cantilever beam. In the conventional CLD, it was found that the shear strain distribution along the VE material was

negligible. On the other hand, the proposed CLD allowed the shear strain to accumulate towards the VE layer's free end, resulting in a damped free vibration response. In addition, the parametric study based on the tubular cantilever beam found that within the considered VE material thicknesses, thinner VE materials generated a higher damping ratio. The study also assessed the longitudinal coverage of the CLD and found that more coverage of the CLD leads to higher damping.

After verifying the ability of the proposed CLD to dampen the vibration on tubular structures, the chapter further studied the effectiveness of the proposed CLD in reducing buffeting-induced vibration on HMIP structures. Covering the bottom 30 ft of the 100-ft tall HMIP added a 1.41% damping ratio to the 0.8% inherent damping of the HMIP, leading to an overall damping of 2.21%. Then, a practical adjustment for the CLD to start above the handhole introduced a 1.08% damping ratio to the HMIP, leading to an overall damping of 1.88%, which is 235% of the HMIP's inherent damping. Finally, the study assessed the dimensionless steady-state response amplitude under the first mode resonance of the HMIP. It was found that the adjusted CLD that starts above the handhole reduced the vibration amplitude by 57.4%, while the CLD that covers the handhole reduced the amplitude by 64% compared to the no CLD case. Overall, the proposed CLD design has shown to be a promising solution for reducing buffeting-induced vibration on HMIPs.

Chapter 4: Conclusions

In this thesis, the primary cause of wind-induced vibrations of HMIP structures was first investigated through long-term field monitoring using a wireless-smart sensor network. The findings from the long-term monitoring period showed that buffeting-induced vibration is the leading cause of HMIP's excessive vibrations. Then, a systematic numerical study was carried out on the effectiveness of using CLDs to reduce buffeting-induced vibrations on the HMIP structures.

In Chapter 2, the preliminary investigation by analyzing the KDOT video recordings of the vibrating HMIPs under wind loading revealed that the HMIP experienced a maximum displacement of around 12 in., and a mode at a frequency of 0.61 Hz dominated the vibration. The dominating mode was confirmed to be the first mode of the HMIP through FE analysis. Subsequently, long-term field monitoring was conducted on a 100-ft tall HMIP in Wakeeney, Kansas. The long-term monitoring found that the HMIP is vulnerable to vibrations induced by vortex shedding and buffeting under wind loading. In particular, by comparing the direction of the vibrations to that of the wind loading and the frequency content of the vibration responses, it was found that buffeting-induced vibrations occurred more often and had greater amplitude than VIV-induced vibrations. The maximum displacement at the top of the HMIP was obtained as 9.5 in. during the Derecho storm in December 2021, demonstrating that buffeting can produce large displacements of the HMP, leading to high-stress demand at the bottom of the structure. Therefore, it was concluded that potential vibration mitigation strategies should focus on reducing the vibration induced by buffeting.

In Chapter 3, the CLDs were investigated to reduce the vibration induced by buffeting on HMIPs in Kansas. First of all, the chapter assessed the conventional CLD on tubular structures

and found that the traditional CLD design that uses one continuous constraining layer around the cylindrical structure was ineffective in reducing the vibration due to the overlapping neutral axes between the base structure and the constraining layer. As a result, the study proposed a new CLD design by adding multiple slits to the constraining layer to divide it into pieces to separate the neutral axis of the base structure from that of the constraining layer. The proposed CLD design allows each piece of the constraining layer to move independently from each other when the structure undergoes bending deformation. Hence, the proposed CLD enables the VE layer to fully engage in shear deformation, dissipating energy for vibration mitigation.

Chapter 3 then investigated three different VE materials by assessing the damping ratios based on a rectangular cantilever beam. The analyses revealed that the Sorbothane VE polymer generated higher damping ratios than both the HDR and the vulcanized natural rubber. Therefore, the Sorbothane VE material was used during the subsequent numerical investigations.

Chapter 3 further compared the conventional and the proposed CLDs in terms of the shear strain distribution along the VE layer based on a prismatic tubular cantilever beam. For the conventional CLD, it was found that the shear strain distribution along the VE material was negligible. On the other hand, the proposed CLD allowed the shear strain to accumulate towards the VE layer's free end, resulting in a damped free vibration response. The result confirmed the effectiveness of the proposed new CLD design. In addition, a parametric study based on the tubular beam was performed and found that among the considered VE layer thicknesses, a thinner VE layer produced higher damping. The study also assessed the longitudinal coverage of the CLD and found that increasing the longitudinal coverage of the CLD leads to better damping performance.

After verifying the ability of the proposed CLD to dampen the vibration on tubular structures, Chapter 3 further studied the effectiveness of the proposed CLD in reducing buffeting-induced vibration on HMIP structures. Numerical results indicated that covering the bottom 30 feet of the 100-ft tall HMIP added a 1.41% damping ratio to the 0.8% inherent damping of the HMIP, leading to an overall damping of 2.21% for the retrofitted HMIP. Then, a practical adjustment for the CLD to start above the handhole introduced 1.08% damping to the HMIP, leading to an overall damping of 1.88%, which is 235% of the HMIP's inherent damping before the retrofit. Finally, the study assessed the dimensionless steady-state response amplitude under the first mode resonance of the HMIP. It was found that compared to the no CLD case, the adjusted CLD that starts above the handhole reduced the vibration amplitude by 57.4%, while the CLD that covers the handhole reduced the amplitude by 64%. Overall, the proposed CLD design has shown to be a promising solution for reducing buffeting-induced vibration on HMIPs.

Future plans of this study mainly include laboratory validation of the proposed new CLD design and its field implementation on a full-scale HMIP structure to verify its efficacy in mitigating buffeting-induced vibrations.

References

AASHTO. (2015). *Design Specifications for Structural Supports for Highway Signs, Luminaires, and Traffic Signals*. American Association of State Highway and Transportation Officials.

ABAQUS. (2021). *ABAQUS/CAE 6.24 User's Manual*. Dassault Systèmes Simulia Corp.

Al-Rumaih, W. S. (2009). *A novel tuned viscoelastic damper for floor vibration abatement* [Ph.D., University of Dayton].

Al-Salih, H. I. A. (2022). *An Investigation of Distortion-Induced Fatigue Cracks in Steel Highway Bridges: From Crack Detection to Fatigue Retrofit* [Ph.D., University of Kansas].

Almarshad, A. (2020). *Structural Health Monitoring Strategies Using Traditional Sensors and Computer Vision* [Ph.D., The University of Kansas].

Almarshad, A., Li, J., & Lepage, A. (2019, August 4-7). *Drift Estimation of Tall Building Structures under Non-stationary Wind Loading through Sensor Data Fusion.* The 9th International Conference on Structural Health Monitoring of Intelligent Infrastructure (ISHMII-9)), St. Louis, Missouri.

Barthelmie, R. J., Wang, H., Doubrawa, P., & Pryor, S. (2016). *Best practice for measuring wind speeds and turbulence offshore through in-situ and remote sensing technologies*. Cornell University.

Caracoglia, L., & Jones, N. P. (2007). Numerical and experimental study of vibration mitigation for highway light poles. *Engineering Structures*, *29*(5), 821-831.

Chen, G., Wang, W., Karim, K. R., & Huang, X. (2012). Dynamic Response Reduction of Cantilevered Columns by Anchored Constrained Viscoelastic Layer Treatments. *Journal of engineering mechanics*, *138*(1), 12-21.

Chen, W., Zhang, Q., Li, H., & Hu, H. (2015). An experimental investigation on vortex induced vibration of a flexible inclined cable under a shear flow. *Journal of Fluids and Structures*, *54*, 297-311.

Desjardins, & McGinn, D. (2018). MODAL ANALYSIS AND DAMPING OF BRIDGE LIGHT POLES. In Proceedings of the CSCE 2018 fredericton annual conference, Canadian Society of civil engineers Fredericton, Canada.

Fu, Y., Hoang, T. A., Mechitov, K., Kim, J. R., Zhang, D., & Spencer, B. F. (2018). Sudden Event Monitoring of Civil Infrastructure Using Demand-Based Wireless Smart Sensors. *Sensors*, *18*(12), 4480.

Hays Regional Station. (2021). *Hays, KS Weather History.* [Weather Report]. Weather Underground. https://www.wunderground.com/history/daily/us/ks/wakeeney/KHYS

Hujare, P., & Sahasrabudhe, A. (2014). Experimental Investigation of Damping Performance of Viscoelastic Material Using Constrained Layer Damping Treatment. *Procedia Materials Science*, *5*, 726-733.

Ibrahim, Y. E., Marshall, J., & Charney, F. A. (2007). A visco-plastic device for seismic protection of structures. *Journal of Constructional Steel Research*, *63*(11), 1515-1528.

Jones, D. I. (2001). *Handbook of viscoelastic vibration damping*. John Wiley & Sons.

Kaczinski, M. R., Dexter, R. J., & Dien, J. P. V. (1998). *Fatigue-resistant design of cantilevered signal, sign and light supports* (Vol. 412). Transportation Research Board.

Kakolvand, H., Ghazi, M., Mehrparvar, B., & Parvizi, S. (2022). Experimental and Numerical Study of a New Proposed Seismic Isolator Using Steel Rings (SISR). *Journal of Earthquake Engineering*, *26*(8), 4000-4029.

Karim, K. R. (2009). *An integrated damping and strengthening strategy for performance-based seismic design and retrofit for highway bridges* [Tech Report]((No. NUTC R165)). Missouri University of Science and Technology. Center for Transportation Infrastructure and Safety.

Karim, K. R., & Chen, G. (2012). Surface damping effect of anchored constrained viscoelastic layers on the flexural response of simply supported structures. *Mechanical Systems and Signal Processing*, *27*, 419-432.

Kliem, M., Høgsberg, J., Vanwalleghem, J., Filippatos, A., Hoschützky, S., Fotsing, E.-R., & Berggreen, C. (2019). Damping analysis of cylindrical composite structures with enhanced viscoelastic properties. *Applied Composite Materials*, *26*(1), 85-113.

Li-Wei Tsai, & Alipour, A. (2020). Assessment of fatigue life and reliability of high-mast luminaire structures. *Journal of Constructional Steel Research*, *170*, 106066.

Li, H., Cheng, J., Sun, W., & Wen, B. (2016). Experimental study on the influence of modal parameters of thin cylindrical shell coated with constrained layer damping. *Journal of Vibroengineering*, *18*(3), 1707-1722.

Li, K. N., & Darby, A. (2009). Modeling a buffered impact damper system using a spring–damper model of impact. *Structural Control and Health Monitoring*, *16*(5), 287-302.

Modhej, A., & Zahrai, S. M. (2021). Numerical study of visco-hyperelastic damper with high axial damping rubber subjected to harmonic loading. *Structures*, *29*, 1550-1561.

Park, J.-W., Sim, S. H., & Jung, H.-J. (2013). Displacement Estimation Using Multimetric Data Fusion. *IEEE/ASME Transactions on Mechatronics*, *18*(6), 1675-1682.

Pirk, R., Rouleau, L., D'Ortona, V., Desmet, W., & Pluymers, B. (2014). Modeling viscoelastic damping insertion in lightweight structures with generalized maxwell and fractional derivative models. 26th International Conference on Noise and Vibration Engineering, Leuven.

Puckett, J., & Ahearn, E. B. (2010). *Reduction of Wind-Induced Vibrations in High-Mast Light Poles* [Tech Report](No. FHWA-WY-10/02F). Wyoming Department of Transportation.

R. M. Young Company. (2000). *Wind Monitor With Voltage Outputs Model 05103V: Instructions*. Traverse city, Michigan: R. M. Young Company.

Reed III, W. H. (1967). Hanging-chain impact dampers-A simple method for damping tall flexible structures. INTERN. RES. SEMINAR-WIND EFFECTS ON BUILDINGS AND STRUCT., Ottawa, Canada.

Shaheen, M., Li, J., Taher, S., Bennett, C., & Collins, W. (2022). Wind-induced vibration monitoring of high mast illumination poles. Sensors and Smart Structures Technologies for Civil, Mechanical, and Aerospace Systems 2022, Long Beach, California.

Sorbothane Inc. (2022). *Sorbothane® Overview*. https://www.sorbothane.com/material-properties.aspx

Zuo, D., & Letchford, C. J. (2008). *Investigation of Wind-Induced Highway Lighting Pole Vibration Using Full-Scale Measurement* [Tech Report]((No. FHWA/TX-08-0-4586-5)). Texas Tech University.